UPDATE: STRUCTURAL UNCERTAINTY OF USED NUCLEAR FUEL IN DRY STORAGE CANISTERS

Fuel Cycle Research & Development

Prepared for
U.S. Department of Energy
Used Fuel Disposition Campaign

Nicholas A Klymyshyn
Philip J Jensen
Nathan P Barrett
Kenneth I Johnson
Marsie Trego
Pacific Northwest National Laboratory

September 16, 2016

FCRD-UFD- 2016-000430
PNNL-25830

Reviewed by:

Project Manager

Brady Hanson (signature on file)
Name

SUMMARY

This report fulfills the M3 milestone M3FT-16PN080203035 "Structural Uncertainty Update" under work package FT-16PN08020303.

The Structural Uncertainty research task uses numerical modeling to help close knowledge gaps associated with extended dry storage of used nuclear fuel. Modeling helps to predict the expected range of mechanical loading on used nuclear fuel and dry storage system components, which is needed to help guide materials research. Knowledge of expected loads helps the materials researchers prioritize their research and focus only on the relevant material degradation phenomena that can have an effect on the ability of dry storage systems to function. The primary loading conditions considered in this task are dry storage cask (DSC) tip-over, handling drops of the multipurpose fuel canister, and seismic loading of DSC systems while situated on the concrete pad of a storage facility.

Loads related to normal conditions of transportation are also relevant to this work, as multipurpose used nuclear fuel canisters are intended to function as dry storage and transportation canisters. The fuel remains sealed within the canister at all times, and in a postulated extended dry storage scenario, intermittent periods of storage and transportation could potentially be moved from one dry storage site to another.

This document is a progress report that describes the work that was performed in fiscal year 2016. The work is a broad task that considers a number of physical phenomena and uses sophisticated LS-DYNA finite element models to predict used fuel and DSC system response to dynamic loads. Due to the broad list of topics and limited budgets, the topics of this task are prioritized at the beginning of the year, and the priorities are subject to revision throughout the year as the Pacific Northwest National Laboratory (PNNL) team collaborates with other members of the Used Fuel Disposition Campaign.

This year's activity on the topic of used fuel modeling focused on performing mechanical dynamic tests on empty fuel cladding and rods that represent the flexural rigidity of used nuclear fuel to gather dynamic data to validate PNNL's detailed fuel assembly model. The fuel assembly model, which represents used nuclear fuel rods as beam finite elements, has been demonstrated to agree reasonably well with shaker and highway test data, but the more controlled environment allows for a closer validation of the numerical model. This level of precise validation is needed as the PNNL detailed fuel assembly model will be used to project the test data recorded in the Equipos Nucleares, S.A./U.S. Department of Energy rail test program from the surrogate fuel used in testing to actual used nuclear fuel.

This year's activity on the topic of multipurpose canister failure mechanisms considered the probabilistic weld failure methodology employed by NUREG-1864 (Malliakos 2007), elastic-plastic fracture mechanics, and stress corrosion cracking. All three of these areas are relevant to modeling the response to dynamic loads and evaluating the model response and assessing the possibility of weld failure. One of the major tasks under Structural Uncertainty is to determine how much material degradation is necessary to threaten the canister containment boundary under normal conditions of handling, storage, and transportation. This research area is still being investigated, but the issues considered this year helped identify areas to focus future work.

This report also summarizes the results of recent modeling work performed to estimate the loads on used nuclear fuel during handling, storage, and transportation. Horizontal package drops of a height that is associated with normal conditions of transport were studied and documented in two conference papers this fiscal year. Another conference paper considered the Sandia truck test and force transmissibility of the conveyance system to project the as-tested loads onto a realistic conveyance system. These papers supplement the analyses that have documented in reports in the past and help establish bounds on the broad range of loading expected on used fuel in handling, storage, and transportation loading conditions.

CONTENTS

SUMMARY iii
ACRONYMS viii
1.0 INTRODUCTION 1
2.0 CLADDING MODELING VALIDATION 3
2.1 Dynamic Test Campaign 3
2.1.1 Pluck Testing 4
2.1.2 Drop Test 8
2.1.3 Shaker Test 12
2.2 LS-DYNA Beam Element Update 12
2.3 Conclusions and Future Work 13
3.0 MULTIPURPOSE CANISTER FAILURE MODELING 15
3.1 Weld Failure Evaluation Using Probabilistic Material Strength Data 15
3.2 Elastic-Plastic Fracture Mechanics Applied to Dynamic Modeling 16
3.2.1 Elastic-Plastic Fracture Methods 17
3.2.2 Plastic Limit Load Analysis 20
3.2.3 Evaluating a Canister Lid Seal Weld Using Elastic-Plastic Fracture and Limit Load Analysis 21
3.3 An Overview of CISCC Research and Methods for Assessing Its Effect on the Structural Integrity of Welded MPCs 25
3.3.1 The Susceptibility and Significance of CISCC on Canister Boundary Integrity . 26
3.3.2 MPC Weld Residual Stress Research 28
3.3.3 Structural Assessment Methods for Canister Normal and Accident Load Conditions 29
3.4 Conclusions and Future Work 33
4.0 USED FUEL LOADING ESTIMATES 34
4.1 NCT Free-Drop Loaded Package Estimate 34
4.2 NCT Highway Transportation Loading Estimate 35
4.3 Normal Conditions of Rail Transportation Loading Estimate 39
4.4 Conclusions and Future Work 39
5.0 CONCLUSIONS 41
6.0 REFERENCES 43

FIGURES

Figure 1: Strain Gauge Location 6in Sample....4

Figure 2: Strain Gauge Location 18in Sample....4

Figure 3: Pluck Test....5

Figure 4: Steel Pluck Tests Results....6

Figure 5: Zirconium Alloy Pluck Test Results....6

Figure 6: Discrete Fourier Transform—Steel Pluck Test....7

Figure 7: Discrete Fourier Transform—Zirconium Alloy Pluck Test....8

Figure 8: Drop Test....9

Figure 9: Drop Test....9

Figure 10: Drop Test Simultaneous Impact—Zirconium Alloy....10

Figure 11: Drop Test Strain Data—Zirconium Alloy....11

Figure 12: Drop Test Discrete Fourier Transform—Zirconium Alloy....12

Figure 13: *J*-integral vs. *J*-resistance Curves for the MPC with an Initial Flaw Depth Equal to 1/3 of the Wall Thickness....19

Figure 14: *J*-integral vs. *J*-resistance Curves for the MPC with an Initial Flaw Depth Equal to 1/2 of the Wall Thickness....19

Figure 15: *J*-integral vs. *J*-resistance Curves for the MPC with an Initial Flaw Depth Equal to 2/3 of the Wall Thickness....20

Figure 16: Membrane Stress at Plastic Collapse vs. Flaw Depth Ratio, a/t....21

Figure 17: Radial Stress History through Canister Lid Seal Weld (Path A to B) during Impact....22

Figure 18: *J*-integral vs. *J*-resistance Curves for Canister Seal Weld under +/-250 MPa Bending Stress....23

Figure 19: Bending Stress in the Uncracked Section that Results in a Plastic Hinge through the Remaining Ligament for the Corresponding Flaw Depth....23

Figure 20: Shear Stress History through the Canister Lid Seal Weld Section during Impact Loading....24

Figure 21: Shear Stress in the Uncracked Section that Corresponds to the 179 MPa Shear Flow Stress in the Remaining Ligament of the Corresponding Flaw Depth....25

Figure 22: Ductility Factor vs. Stress Triaxiality Factor (Manjoine 1982)....31

Figure 23: The Ductility Factor Compared to 1/TF and the 0.67/TF Limit Proposed by Snow et al. (2009) for the ASME Code....32

Figure 24: Scaled and Original Acceleration Time History....36

Figure 25: Isometric View Showing Mesh 37
Figure 26: Rod Length and Loading Locations 37

TABLES

Table 1: Type 308 Stainless Steel Weld Material Probabilistic True Strain at Failure Data from NUREG-1864 16
Table 2: Flexural Rigidity (EI) and Elastic Moduli...38
Table 3: Axial Strains, Peak Deflection, Shear Force, and Bending Moment 39

ACRONYMS

ASME	American Society of Mechanical Engineers
CISCC	chloride induced stress corrosion cracking
DOE	U.S. Department of Energy
DSC	dry storage cask
EI	flexural rigidity
ENSA	Equipos Nucleares, S.A
EPRI	Electric Power Research Institute
FMEA	Failure Modes and Effects Analysis
FY	fiscal year
MPC	multipurpose canister
NADP	National Atmospheric Deposition Program
NCT	normal conditions of transport
NRC	U.S. Nuclear Regulatory Commission
PNNL	Pacific Northwest National Laboratory
RA	reduction of area
SCC	stress corrosion cracking
SNL	Sandia National Laboratories
TSF	true strain to failure
UFDC	Used Fuel Disposition Campaign
UNF	used nuclear fuel

UPDATE: STRUCTURAL UNCERTAINTY OF USED NUCLEAR FUEL IN DRY STORAGE CANISTERS

1.0 INTRODUCTION

Used nuclear fuel (UNF) storage and transportation pose a number of technical challenges. One of the major challenges is uncertainty in material behavior over extended periods of time. Although some literature exists on the properties of UNF after coming out of the reactor environment, significant uncertainty still exists in the performance of UNF and its storage and transportation systems (canister and internals) during extended periods. The goal of the Structural Uncertainty research task is to determine the amount of material degradation that is permissible in dry storage cask (DSC) system components under extended dry storage scenarios. The value of this numerical modeling study is to provide guidance to materials researchers on what material degradation phenomena require study. The ultimate purpose of this task is to assist in filling a knowledge gap in the realm of extended dry storage of UNF.

This report documents the progress the Pacific Northwest National Laboratory (PNNL) made during fiscal year 2016 (FY16) and identifies the work that remains to be completed in future years. This research task began with a study of the structural sensitivity of DSC systems to dry storage mechanical loading scenarios presented in Klymyshyn et al. (2013). The task continued in 2014 with a focus on fuel assembly response in Klymyshyn et al. (2014a). In 2015, this task area studied cladding modeling options, the potential effect of cladding thinning, and stress corrosion cracking of the multipurpose canister welds under dynamic loads in Klymyshyn et al. (2015a). In 2016, PNNL completed a study of a 30 cm rail package handling drop, which represents a normal conditions of transport (NCT) load case (Klymyshyn 2016a).

This year, three major topics were explored. UNF modeling using classic beam finite element representation under dynamic loading conditions is discussed in Section 2.0. Methods to model failure in UNF canisters are discussed in Section 3.0. The current range of loading on UNF rods based on recent modeling is discussed in Section 4.0. Conclusions and recommendations for future work are discussed in Section 5.0.

2.0 CLADDING MODELING VALIDATION

PNNL uses a highly detailed fuel assembly model to evaluate the response of used fuel to a variety of dynamic loading conditions that occur during storage and transportation. Examples include shaker table and truck testing (Klymyshyn et al. 2014b), rail transportation (Adkins et al. 2013), and dry storage loading conditions (Klymyshyn et al. 2014a). The detailed fuel assembly model was also used in transportation package free drop modeling studies that are discussed in more detail in Section 4.0. The fuel assembly model will also be used to support the upcoming Equipos Nucleares, S.A./U.S. Department of Energy (ENSA/DOE) rail and intermodal test campaign and will ultimately be used to simulate the loading environment recorded during testing in order to determine the response of real UNF to help close the Used Fuel Disposition Campaign (UFDC) stress profiles knowledge gap.

The importance of this model to the UFDC program necessitates a certain level of validation. Shaker table and highway test data provides some specific validation cases. In general, the LS-DYNA fuel assembly model agrees well with recorded strains to roughly the third or fourth decimal point (i.e., 0.001 or 0.0001) under complex full fuel assembly dynamic loading conditions. Maximum recorded strains that have been recorded during NCT testing have tended to be in the fourth significant digit (e.g., 0.000150), so achieving better accuracy and precision in LS-DYNA models would be desirable if it can be done. In FY15, PNNL studied options available within LS-DYNA to model cladding to achieve the best agreement with classic closed form solutions of stress and strain under quasi-static bending loads (Klymyshyn et al. 2015b).

This FY, PNNL performed dynamic mechanical testing of fuel cladding and surrogate steel rods to develop a database of test data to benchmark and validate the LS-DYNA fuel rod behavior. The data was collected under controlled conditions and will be used in the future to study the accuracy of the LS-DYNA code and test alternate finite element modeling options to achieve greater agreement with physical test results. The mechanical testing is described in Section 2.1.

Modeling used fuel using beam elements is an ongoing area of study. The goal is to model the used fuel effectively in LS-DYNA, with a level of accuracy that fits the results. Section 2.2 discusses some LS-DYNA beam element observations from this year.

2.1 Dynamic Test Campaign

To validate portions of the numerical models described herein, staff at PNNL have performed a series of dynamics tests. The test series includes pluck, drop, and shaker testing. These tests are performed on 6in and 18in samples of zirconium alloy tubing and on 3/8in steel rod, which approximates the flexural rigidity (EI) of bonded UNF. Strain gauges are mounted on the samples in the axial and circumferential directions. The location of the strain gauges for the 6in and 18in samples are shown in Figure 1 and Figure 2 respectively.

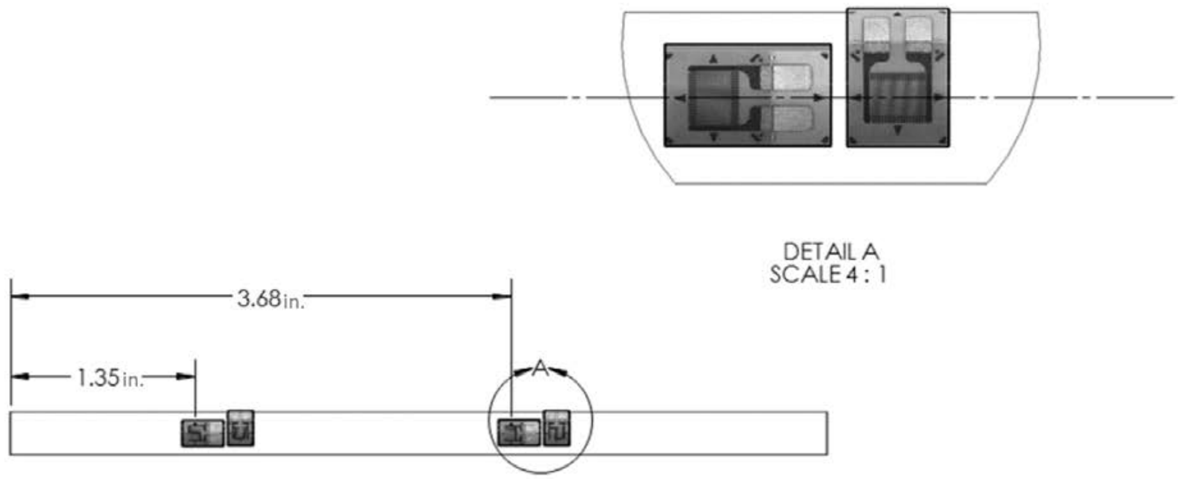

Figure 1: Strain Gauge Location 6in Sample

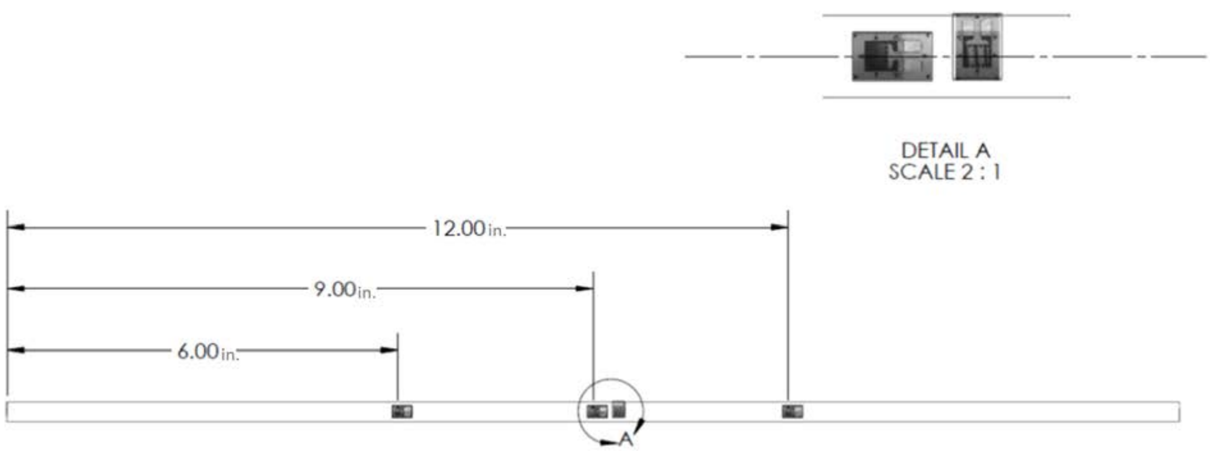

Figure 2: Strain Gauge Location 18in Sample

Each strain gauge was connected to a Vishay 2310 instrumentation amplifier with a quarter Wheatstone bridge. The instrumentation amplifier output was recorded with DATAQ® DI-2108 data logger capable of recording eight channels at maximum of 50 kHz.

2.1.1 Pluck Testing

The pluck tests are performed by clamping the 6in samples in a 1in clamp mounted on the cross head of the load frame (Figure 3). The free end of the cantilever beam is held against a pinned clevis and the sample is precisely deflected by moving the clamping block attached to the load frame crosshead. Each sample is deflected 0.0625in, which is small enough to ensure that the sample does not plastically deform. The pluck test is initiated by quickly removing the clevis pin to start the vibrating beam response. The oscillating strains are recorded by the data acquisition system.

The pluck test is shown in Figure 3. The end of the cantilever is denoted by arrow 1. At this location, the PNNL team verified the deflection with a micrometer. The micrometer is also used after every test to verify that the cantilever returned to its original position; this indicates that no plastic deformation occurred. Arrow 2 indicates the mid-span strain gauges; during testing, these are denoted as “far bending” and “far circumferential.” Arrow 3 indicates the clamped end strain gauges; during testing, these are denoted as “near bending” and “near circumferential.”

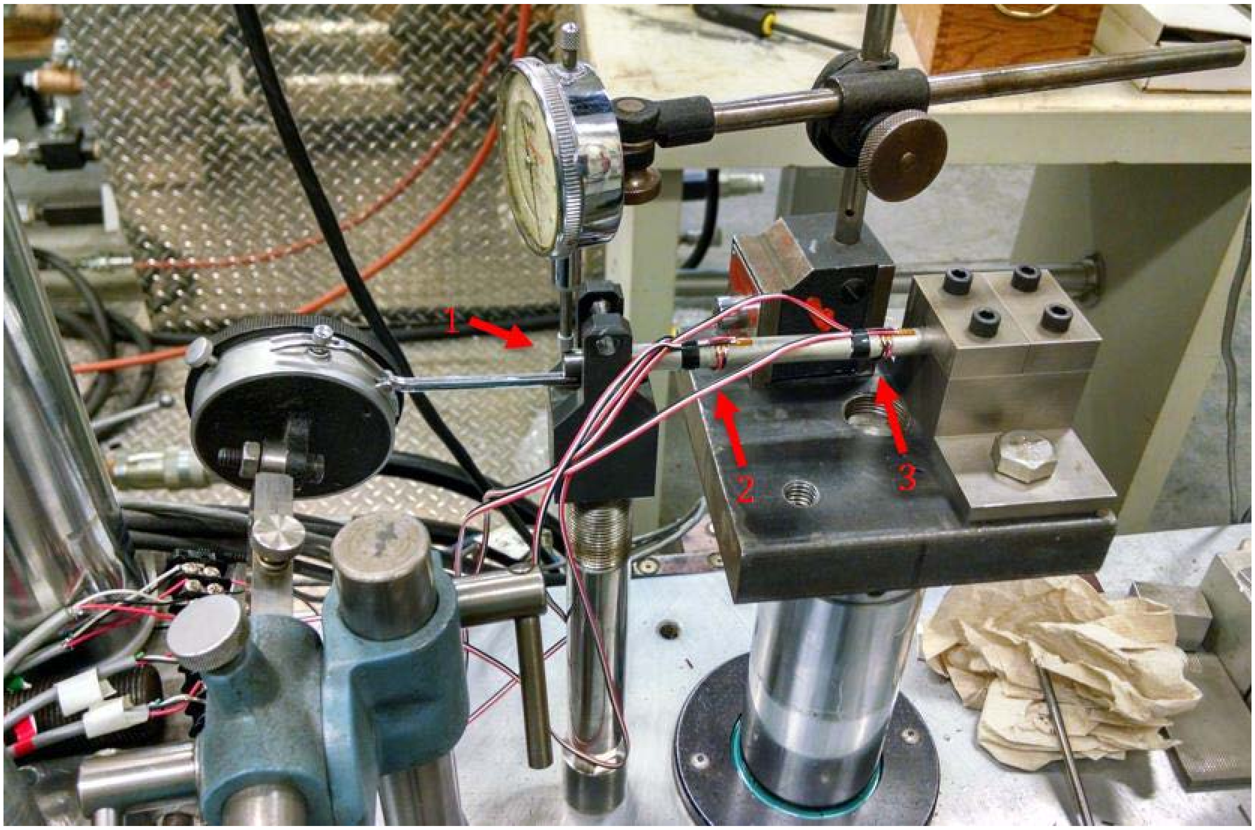

Figure 3: Pluck Test

The results from the steel pluck test are shown in Figure 4. Two plots are shown. The first displays the entire strain time history, and the second displays the strain in the steel rod after the rod has been plucked.

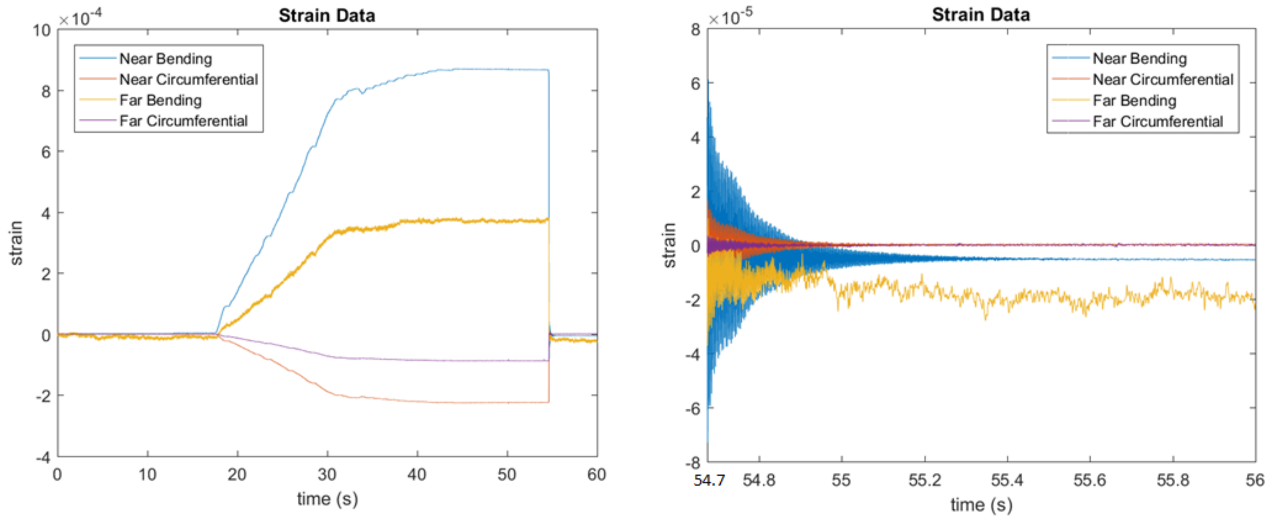

Figure 4: Steel Pluck Tests Results

The results from the zirconium alloy pluck test are shown in Figure 5. Two plots are shown. The first displays the entire strain time history, and the second displays the strain in the cladding segment after the rod has been plucked.

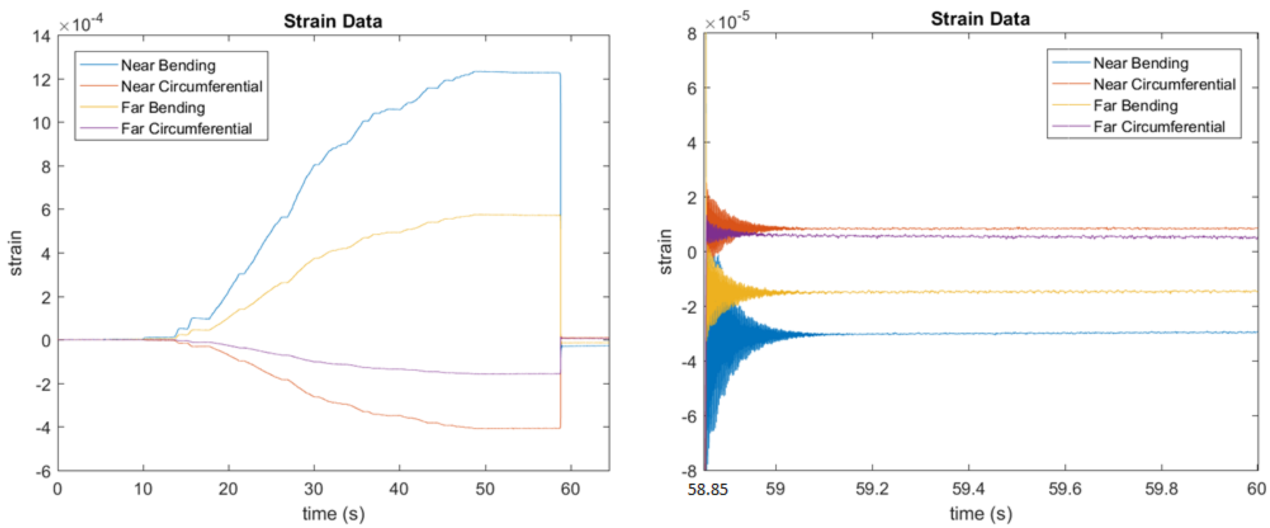

Figure 5: Zirconium Alloy Pluck Test Results

Figure 6 and Figure 7 display the discrete Fourier transform of the steel pluck test and the zirconium alloy pluck test, as calculated using MATLAB. Figure 6 shows that the measured natural frequency of the steel rod is approximately 317.7 Hz, and Figure 7 shows that the measured natural frequency of the zirconium alloy tube is 391.6 Hz. For comparison, the natural frequency of a clamped cantilever can be calculated using equation 1 (Roark and Young, 1975), which yields 350 Hz for the steel rod and 425 Hz for zirconium alloy tube. The difference between experimentally determined natural frequencies and the theoretical closed form solution results is expected to be caused by the practical conditions of testing, such as compliance in the test fixture and naturally occurring damping in the test environment.

$$f_i = \frac{K_1}{2\pi}\sqrt{\frac{EI}{\rho A L^4}}, \qquad K_1 = 3.52 \tag{1}$$

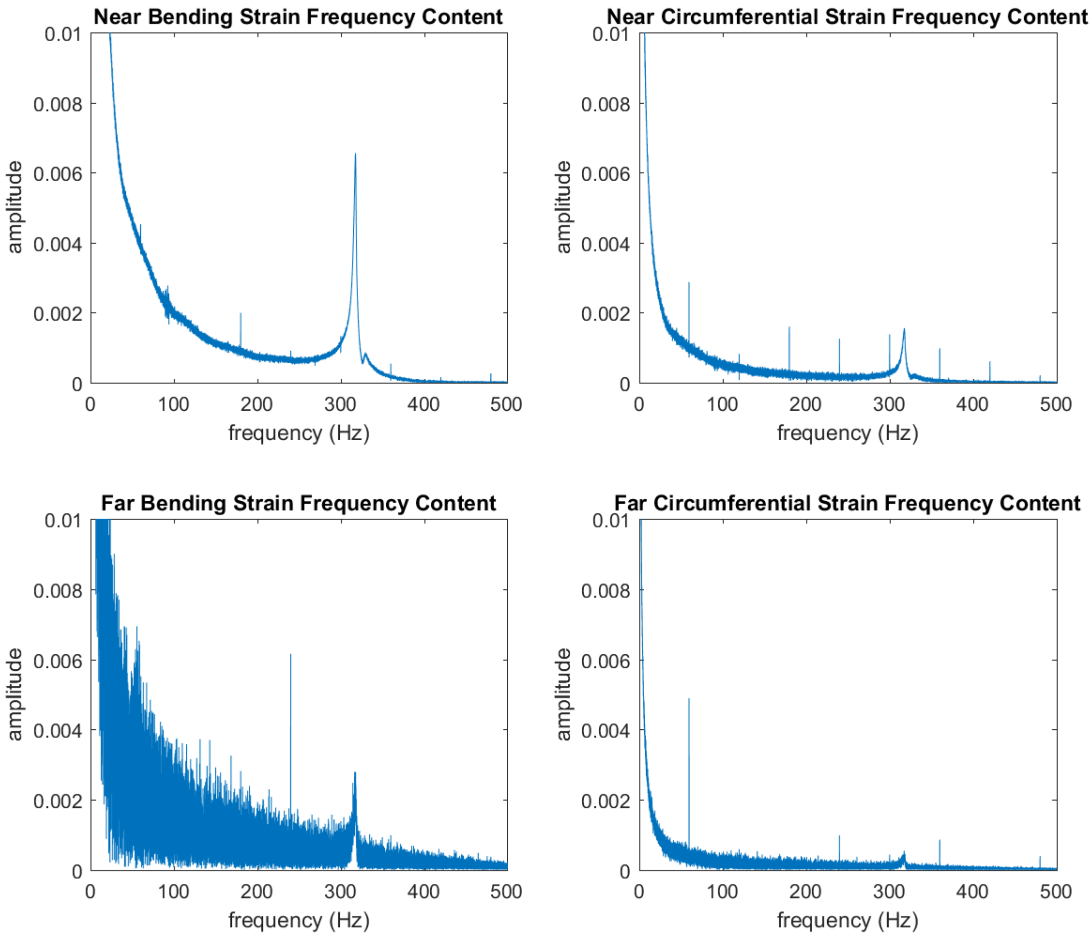

Figure 6: Discrete Fourier Transform—Steel Pluck Test

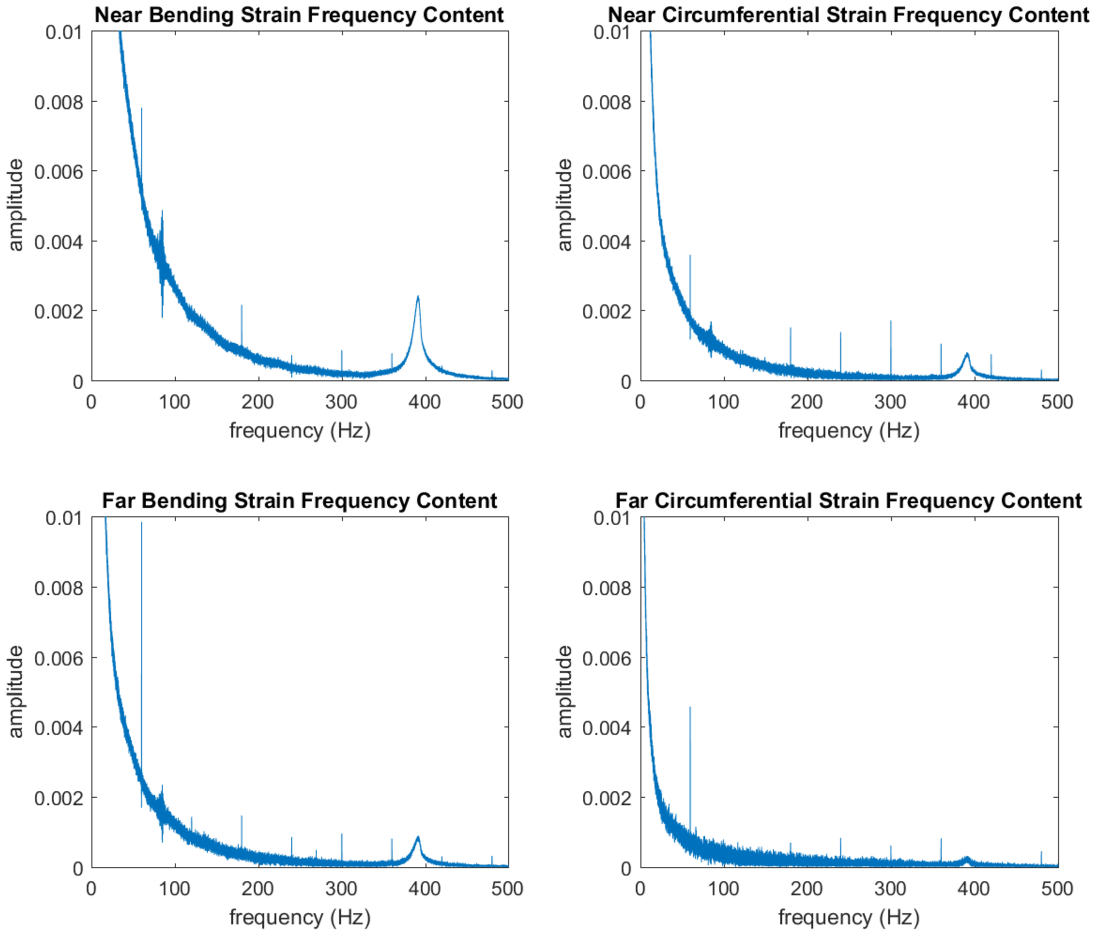

Figure 7: Discrete Fourier Transform—Zirconium Alloy Pluck Test

2.1.2 Drop Test

The drop test consists of an 18in steel rod or zirconium rod, as shown in Figure 2, dropped from a height of 1ft to 5ft, and onto two rods spaced 8in to 17in apart. The impact is recorded using a 500 frames-per-second high-speed camera. The drop test is shown in Figure 8 and Figure 9.

Figure 8: The Drop Test Setup

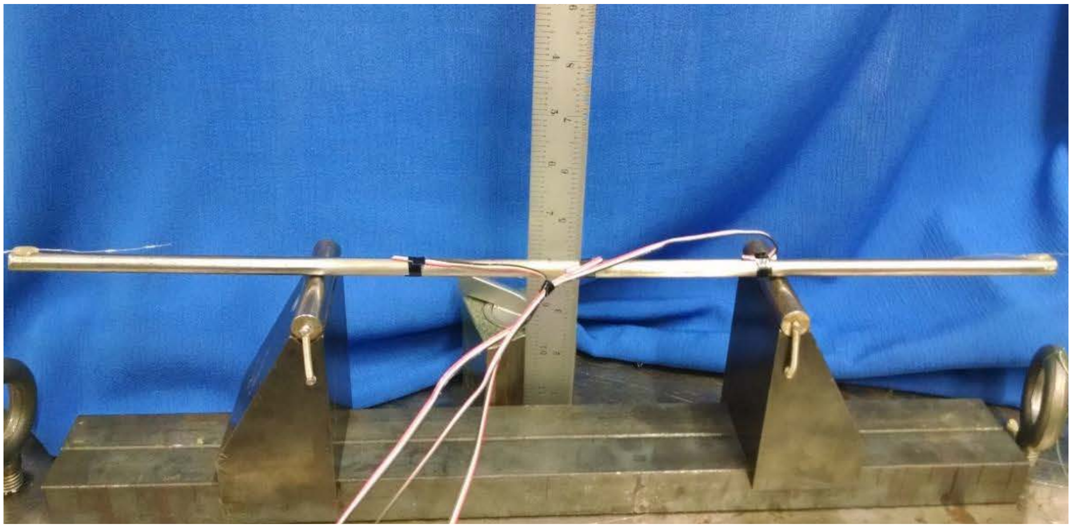

Figure 9: Close up of Drop Test Impact Zone

Figure 10 shows a zirconium alloy rod impacting the target rods simultaneously. Testing included drops in which the left target rod was impacted first, the right target rod was impacted first, and both target rods were impacted simultaneously.

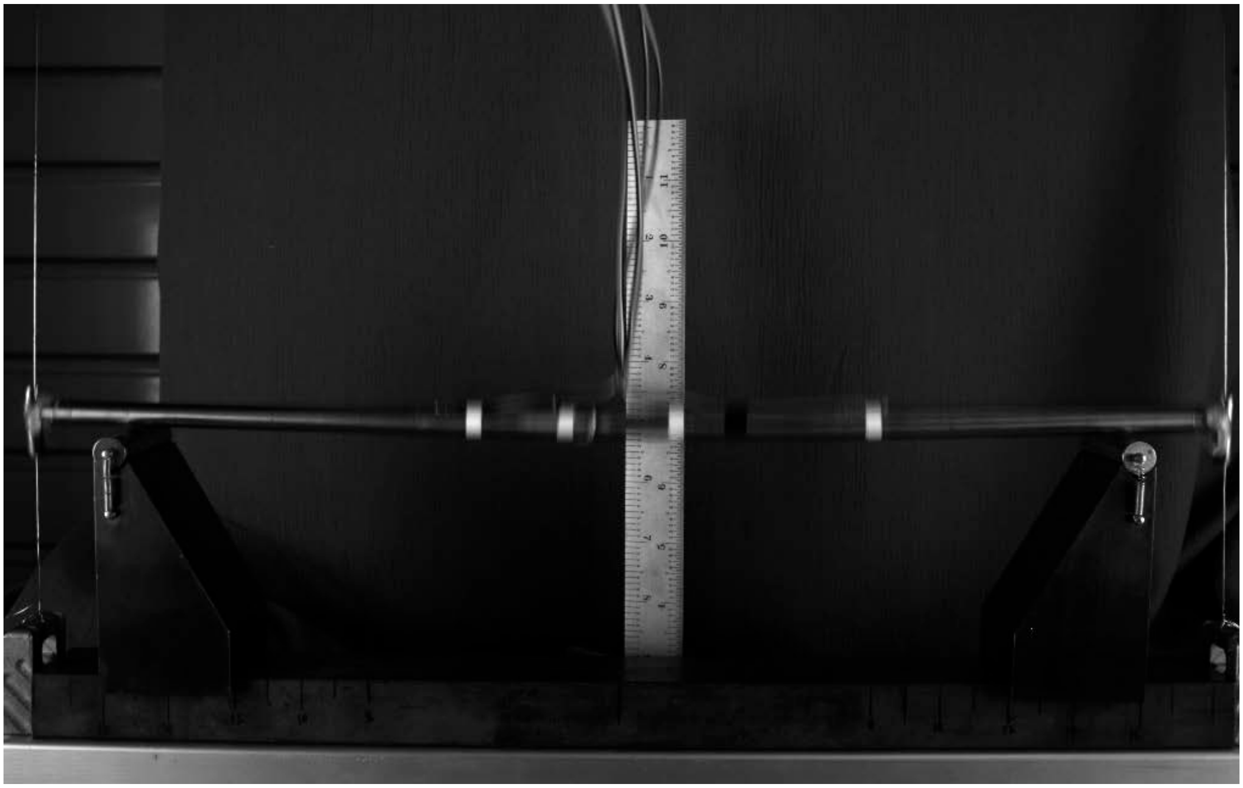

Figure 10: Drop Test Simultaneous Impact—Zirconium Alloy

Figure 11 shows the strain data recorded from the drop shown in Figure 10. In Figure 11, the moment of impact can be clearly seen in the strain data; after the initial impact, a secondary impact was also recorded.

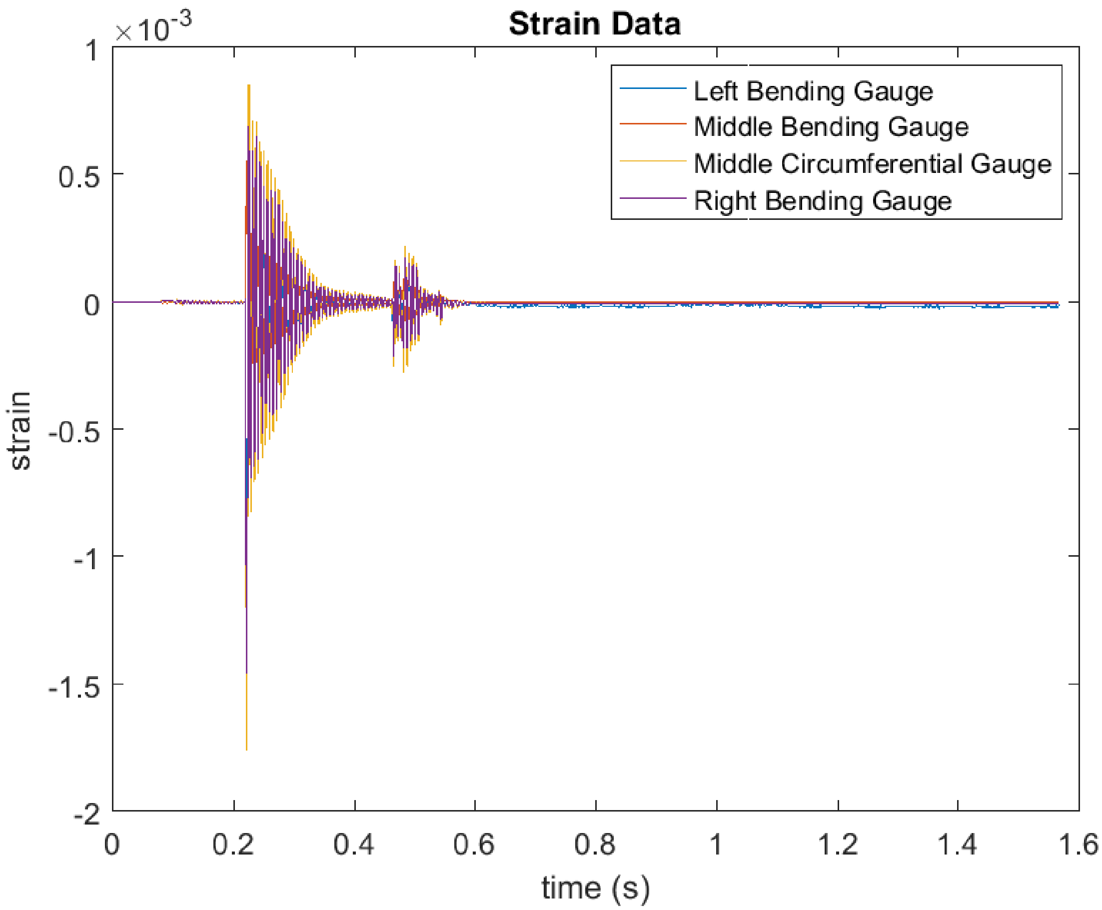

Figure 11: Drop Test Strain Data—Zirconium Alloy

Figure 12 shows the discrete Fourier transform of the strain data shown in Figure 11. In Figure 12, all four strain gauges recorded a peak at approximately 158.9 Hz, and the left and right strain gauges recorded a second peak at approximately 456.1 Hz.

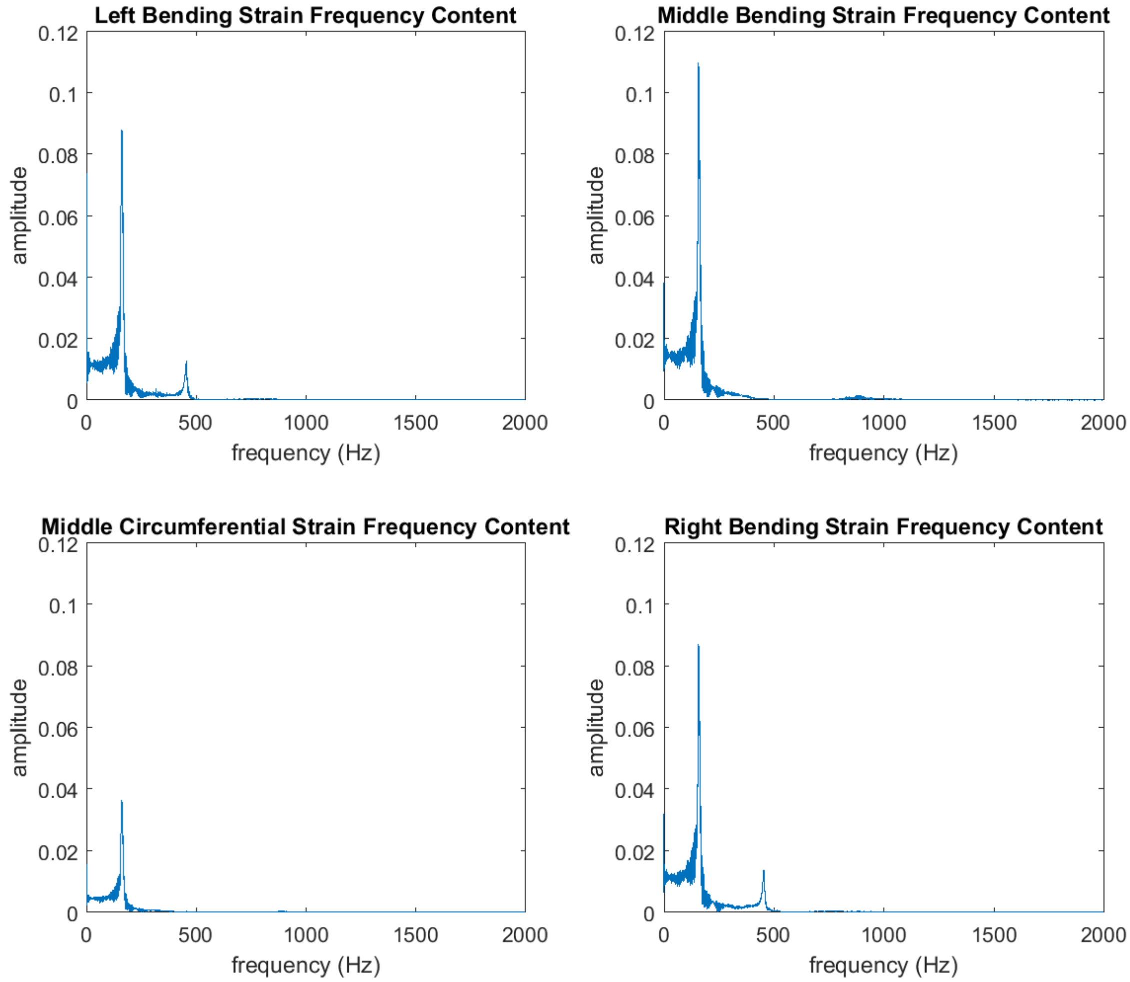

Figure 12: Drop Test Discrete Fourier Transform—Zirconium Alloy

2.1.3 Shaker Test

PNNL is currently pursuing shaker testing with 6in and 18in specimens. This testing will consist of clamping each specimen in a clamped-free and clamped-clamped configuration. The shaker table acceleration and the specimen strain will be recorded. This work is currently ongoing, and results will be available in FY17.

2.2 LS-DYNA Beam Element Update

Currently, PNNL is still using the default Hughes-Liu beam element formulation with 2x2 Gauss quadrature as the standard way to model UNF. This is the default beam element setting in LS-DYNA, and it tends to provide the fastest results in large, complex fuel assembly finite element models. PNNL will continue to use this beam model for consistency until a clear case is made to change it.

The Belytschko-Schwer integrated beam element formulation with 4x4 Gauss quadrature was demonstrated to have slightly better agreement with closed form solution results for quasi-static bending, but this has not yet been evaluated under dynamic loading conditions. The dynamic test data described in Section 2.1 will be used in future work to compare the behavior of these element formulation options.

The 3x3 Lobotto quadrature was used in the single rod model discussed in Section 4.2. This quadrature rule affects the location of integration points in the beam cross section. The Lobotto 3x3 option locates nine integration points around the outer perimeter of the beam cross section in 40-degree increments. The 3x3 option is potentially a better quadrature rule than the 2x2 or 4x4 Gauss quadrature because they locate integration points at the mid-thickness of a tube, and the main interest is at the outer surface where bending strains are maximized. When tubular cross sections are used, the difference in mid-cladding strain and outer surface strain is only about 6% in pure bending. The difference becomes much greater when a solid cross section is used, up to a 100% difference. Solid and tubular beam cross sections are both viable options because the primary behavior of interest is bending, and the fuel rods are assigned modulus and cross section properties to achieve a target EI.

The quadrature rule affects the number and location of integration points, which are the locations where the stress, strain, and all other results are calculated. When the integration points are not located at a desired location, bending moment, axial force, and other results quantities can be used to calculate strain at a particular location, such as at the outer surface. The package drop analyses of Section 4.1 discovered that strains calculated from bending moments were 40% to 51% higher than integration point strains. This result is an issue to explore in future comparison models because the strains derived from the two methods are expected to be approximately equal.

2.3 Conclusions and Future Work

The mechanical test data collected this year will be used in the future to help validate the LS-DYNA beam elements used to represent UNF rods in PNNL's detailed fuel assembly models. A number of beam formulations and quadrature rules are available. PNNL will also investigate the difference between using integration point strain data directly and calculating strain from bending moment and other results data. In theory, integration point strains and strains derived from beam loading information should be equal, but examples show 40% to 51% difference. As the PNNL models may be relied on to close the stress profiles knowledge gap, the uncertainties and limitations of the finite element analyses must be fully understood.

3.0 MULTIPURPOSE CANISTER FAILURE MODELING

One of the key topics of the structural uncertainty task is to determine the conditions that can cause failure in a multipurpose canister during long-term storage. Predicting failure is not a standard engineering concern; instead, structures are typically designed to withstand a certain level of loading by demonstrating compliance with conservative stress limits. Design codes, such as American Society of Mechanical Engineers (ASME) *Boiler and Pressure Vessel Code*, establish stress limits that generally require steel structures to remain elastic during normal operation and only permit plastic deformation under accident conditions, where the structure may be required to maintain its pressure-retaining boundary but would not be expected to be used again after the accident is over.

One way to consider the potential for failure in a dynamic loading scenario is to consider material test data based on samples taken from real structures that have experienced some period of actual service. NUREG-1864 (Malliakos 2007) is a probabilistic risk assessment of a dry cask storage system that used material test data for samples of Type 304 stainless steel and Type 308 stainless steel weld filler material to establish a material failure strength probability distribution. The NUREG used its probabilistic failure strength distribution to determine a probability that the calculated dynamic loads on a canister weld would exceed the material failure strength. This methodology is discussed in more detail in Section 3.1.

Another way to consider multipurpose canister (MPC) failure is with elastic-plastic fracture mechanics. This analytical methodology assumes a flaw (e.g., a crack in the weld material) exists at a location and determines if the calculated loading is sufficient to cause a crack to propagate through the wall. While it is typically applied to static loading scenarios, this type of analysis can be used to determine a minimum flaw size that can challenge the MPC integrity. This methodology is discussed in more detail in Section 3.2.

The development of cracks in MPC welds is a current technical concern for long-term dry storage. This report provides an overview of chloride induced stress corrosion cracking (CISCC) issue as it relates to dry storage of UNF within MPCs. Current research work is summarized in Section 3.3 to identify the potential for and the consequences of this degradation mechanism to assess how it should be included in structural integrity evaluations of MPCs.

3.1 Weld Failure Evaluation Using Probabilistic Material Strength Data

The potential for weld failure in a used fuel dry storage system was evaluated in NUREG-1864 (Malliakos 2007) using explicit finite element models to calculate the accumulated plastic strain in a canister weld region and comparing it to a material strain at failure. The true strain at failure (TSF) was determined from test data taken from samples of fabricated weldments from multiple sources. The test data was used to construct a probabilistic relationship for TSF, assuming a normal distribution. The TSF values and their statistical data presented in NUREG-1864 are reported in Table 1 for the purpose of discussion. Section 3.3.3 covers the application of this TSF data in more detail.

Table 1: Type 308 Stainless Steel Weld Material Probabilistic True Strain at Failure Data from NUREG-1864

Standard Deviation From Mean	True Strain at Failure (TSF)	Probability that TSF Is Less Than the Tabulated Value
0.0 (mean)	0.73	0.5000
0.5	0.64	0.3085
1.0	0.55	0.1587
1.5	0.47	0.0668
2.0	0.40	0.0228
2.5	0.32	0.0062
3.0	0.26	0.0013
3.5	0.20	0.00023
4.0	0.14	0.000032
4.5	0.087	0.000003
5.0	0.036	<0.000001

Table 1 describes a probabilistic representation of the observed material failure behavior of the Type 308 stainless steel. The test data is fit to the normal probability distribution, which is a continuous distribution that is likely defined well beyond the range of the available test data. In this probability distribution, the two standard deviation TSF value of 0.40 means that there is only a probability of 0.0228 (i.e., less than 3% chance) that the TSF at a particular location of interest will turn out to be lower than 0.40. A 95% confidence level is typically sufficient for engineering purposes, but the normal distribution defines the TSF out to very low probabilities that do not necessarily match the test data. For example, the five standard deviation value of TSF = 0.036 represents a probability that has less than a one in a million chance of occurring. To truly test material behavior out to this level of probability would require on the order of a million samples.

This statistical representation of TSF is interesting, but it is not clear where the assumption of a normal distribution ceases to be valid. For example, does the five standard deviation TSF value of 0.036 represent a valid, credible low probability TSF? It is recommended that the source data be reviewed to determine the actual minimum documented TSF value recorded during testing and to see if a better statistical model of the data is available.

3.2 Elastic-Plastic Fracture Mechanics Applied to Dynamic Modeling

The 304 and 316 stainless steels used to construct MPCs for spent fuel containment are highly ductile alloys such that flaw growth typically occurs by elastic-plastic fracture or net section plastic limit load. This section summarizes the elastic-plastic fracture and plastic collapse failure mode calculations to compare which will govern in the growth and failure of stress corrosion cracking (SCC)-induced flaws in the wall of an MPC.

3.2.1 Elastic-Plastic Fracture Methods

PNNL performed an elastic-plastic fracture analysis to calculate the canister wall stress at which unstable crack growth would be predicted. The analytical solution for a cylinder with an internal circumferential crack was used to calculate the applied *J*-integral as a function of crack depth and applied axial stress. The applied *J*-integral curves for increasing stress levels were compared with the *J*-resistance curve for 304 stainless steel to estimate 1) the applied stress where fracture would initiate and 2) whether or not the crack would arrest or grow through-wall. Kumar et al. (1981) provide a detailed discussion of the *J*-estimation methods for this analysis. The total *J*-integral is the sum of the elastic and plastic components of *J*.

$$J = J_e + J_p \tag{2}$$

$$J_e = K_I^2 \frac{\left(1-\nu^2\right)}{E} \tag{3}$$

$$J_p = \alpha\sigma_0\varepsilon_0 c(a/b)H(a/b,n)\left(\frac{P}{P_0}\right)^{n+1} \tag{4}$$

where:

- K_I is the stress intensity factor from linear elastic fracture mechanics
- ν is the Poisson's ratio
- E is the elastic modulus
- $\alpha, \sigma_0, \varepsilon_0, n$ are the parameters of the Ramberg-Osgood stress-strain curve
- a = flaw depth, b = wall thickness, and c = remaining ligament (b-a)
- $H(a/b,n)$ is the plastic *J* influence function as a function of crack depth and the Ramberg-Osgood exponent, n
- $\left(\frac{P}{P_0}\right)^{n+1}$ is the ratio of the applied load P to the perfectly plastic limit load, P_0.

Kumar et al. (1981) provide the plastic *J* influence functions, $H(a/L,n)$, for the following geometries that are important to evaluating flaws in used fuel containers:

- Internally pressurized cylinder with an internal axial crack
- Cylinder with an internal circumferential crack under remote tension

- Single-edge cracked plate in uniform tension
- Single-edge cracked plate in three-point bending

Ji et al. (1993) extended the flawed cylinder solutions to R/t=40. The above cracked geometries can be used to approximate the elastic-plastic fracture of flaws in various orientations in used fuel canisters. Due to the stiffening effect of the cylindrical geometry, the solution for the internal circumferential flaw can also be used to approximate a cylinder with external flaws.

Kumar et al. (1981) also provide the Ramberg-Osgood stress-strain parameters for 304 stainless steel plus a detailed example of how the *J*-estimation method was applied to circumferential cracking of a large cylinder under axial loads.

Klymyshyn et al. (2015) reproduced the example in Kumar et al. (1981) and then modified the calculation to evaluate cracking in the wall of an MPC. *J*-resistance curves were compiled from the literature for 304 stainless steel to find the lower-bound curve for use in the analysis. The literature showed that static loads typically result in lower *J*-resistance than impact loads. Therefore, the lower-bound *J*-resistance curve measured by Sampath et al. (1981) with static three-point bend tests was used in the analysis.

The *J*-integral evaluation for the MPC was conducted by substituting the canister body dimensions (86.4 cm inner radius and 12.7 mm) into the spreadsheet used for the example calculations. Figures 13 through 15 show the calculated *J*-integral vs. *J*-resistance curves for initial flaw depths of 1/3, 1/2, and 2/3 of the canister wall thickness, respectively. These initial depths were chosen because the canister welds are often made in two or three weld passes. The *J*-integral curves that intersect and cross below the *J*-resistance curve correspond to tensile stress values in the cylinder body that would result in stable crack growth from the initial crack depth to the increased depth where the *J*-integral and *J*-resistance curves first intersect. Using this criterion, the tensile stress curves below 330 MPa in Figure 13 would result in a small amount of stable crack growth. The blue curve at 350 MPa does not intersect the *J*-resistance curve, and therefore an applied stress of 350 MPa would result in unstable crack growth.
Figure 14 shows that 250 MPa is the limit for stable crack growth if the initial flaw depth is 1/2 the wall thickness. Figure 15 shows that 183 MPa is the limit for stable crack growth if the initial flaw depth is 1/3 the wall thickness.

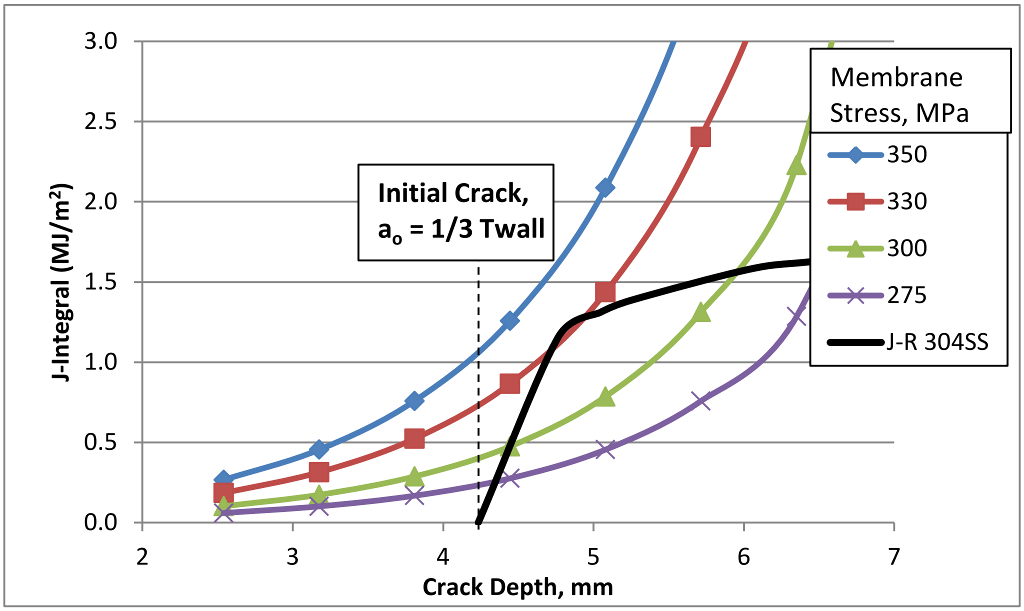

Figure 13: *J*-integral vs. *J*-resistance Curves for the MPC with an Initial Flaw Depth Equal to 1/3 of the Wall Thickness

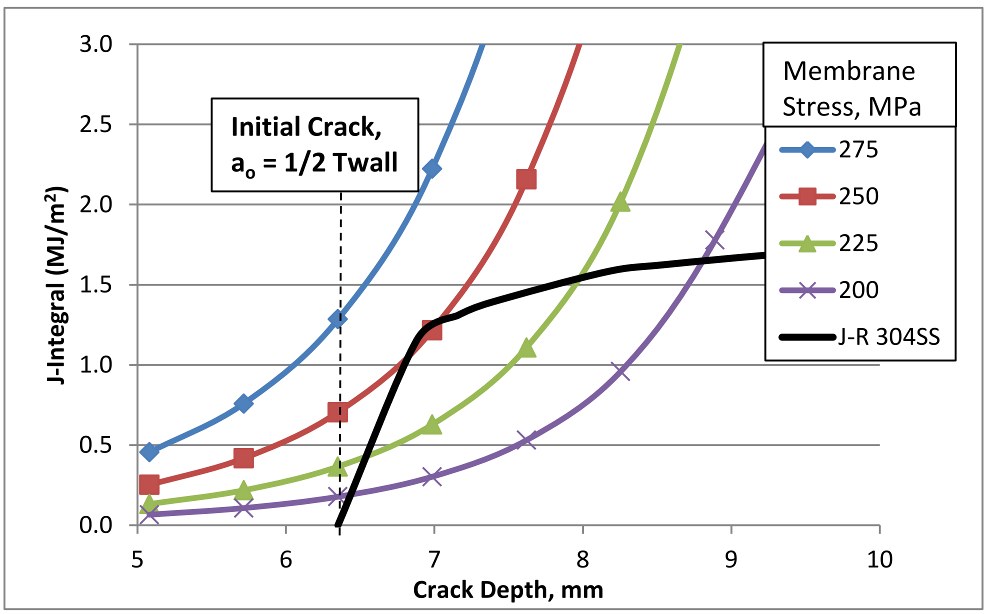

Figure 14: *J*-integral vs. *J*-resistance Curves for the MPC with an Initial Flaw Depth Equal to 1/2 of the Wall Thickness

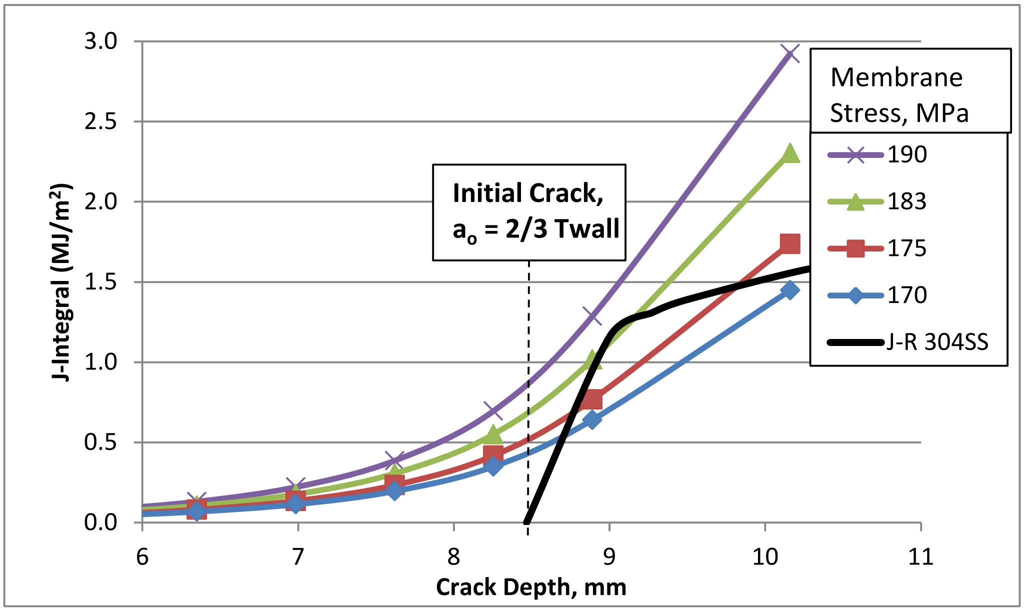

Figure 15: *J*-integral vs. *J*-resistance Curves for the MPC with an Initial Flaw Depth Equal to 2/3 of the Wall Thickness

3.2.2 Plastic Limit Load Analysis

The plastic limit load failure criteria in Section XI, Appendix C of the *ASME Boiler and Pressure Vessel Code* (ASME 2013a) can be used to estimate the flaw depth at plastic collapse that corresponds to the material flow stress in the cylindrical canister body. For a full circumferential crack, the membrane stress, σ_m, at incipient plastic collapse is expressed as:

$$\sigma_m = \frac{\sigma_f}{SF_m}\left(1 - \frac{a}{t}\right) \quad (5)$$

where,

SF_m = Structural safety factor for service levels A-D, SF_m(D) = 1.3
SF_m = 1.0 at incipient collapse
σ_f = flow stress $= \dfrac{\sigma_y + \sigma_u}{2}$
σ_y = yield stress
σ_u = ultimate stress
a = through thickness crack depth
t = vessel wall thickness

Rearranging equation (5), the maximum allowable crack depth of a full circumferential crack at incipient limit load failure is equal to

$$\frac{a}{t} = \left(\frac{\sigma_f - SF_m \sigma_m}{\sigma_f} \right) \tag{6}$$

The minimum yield and ultimate strengths of 304 stainless steel at room temperature are listed as 172 MPa (25 ksi) and 448 MPa (65 ksi) in Section II of the ASME code (ASME 2013b). This gives a flow stress of 310 MPa (45 ksi). Equation (6) provides a conservative estimate of the maximum flaw depth for plastic collapse at the tensile stress, σ_m, for unstable crack growth that was calculated in the elastic-plastic fracture analysis. For a given applied stress, σ_m, plastic collapse would be expected to occur before the onset of unstable crack growth if the flaw depth for plastic collapse is less than the flaw depth for unstable elastic-plastic fracture.

Equation (5) also gives the tensile membrane stress at plastic collapse as a function of the flow stress and the ratio of flaw depth to thickness. Figure 16 shows that for a flow stress of 310 MPa, the average membrane stress (in an uncracked section) at incipient plastic failure is only 210 MPa, 155 MPa, and 100 MPa for initial flaw depths of 1/3, 1/2, and 2/3 wall thickness, respectively. These are lower than the maximum stresses for elastic-plastic fracture (Figure 13 through Figure 15), which suggests that the ductile stainless steel of the canister body would deform plastically without crack extension.

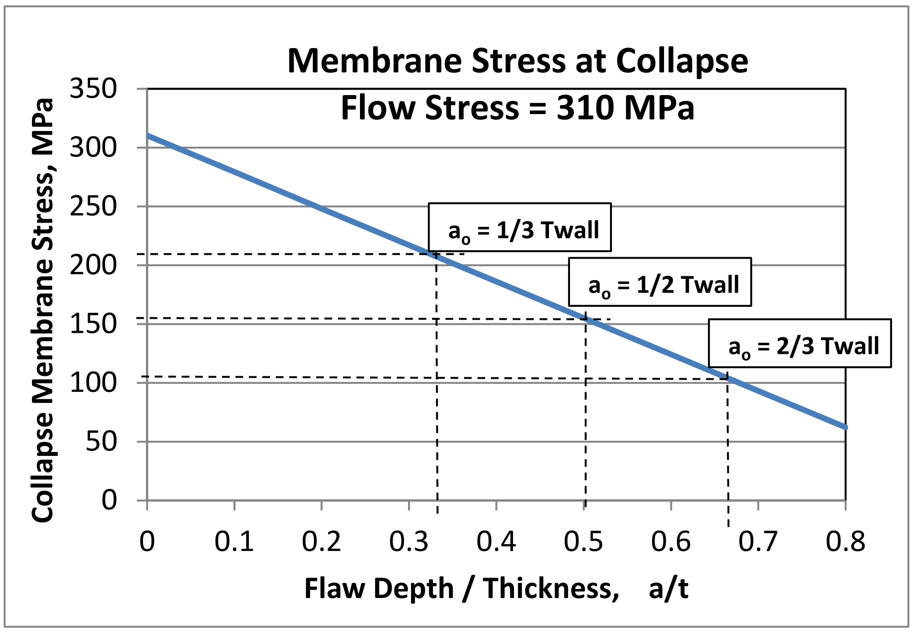

Figure 16: Membrane Stress at Plastic Collapse vs. Flaw Depth Ratio, a/t

3.2.3 Evaluating a Canister Lid Seal Weld Using Elastic-Plastic Fracture and Limit Load Analysis

A second example is given where the dynamic stresses through a canister lid seal weld are evaluated for an end-on impact event. The loading conditions represent a loaded MPC experiencing a handling drop event when being loaded into a dry storage overpack. An LS-DYNA model calculates the response of the MPC during the drop event. Figure 17 shows the stress history in the radial direction through the lid seal weld (points A and B). The peak stresses in the weld section were evaluated to estimate the governing critical flaw size using the elastic-plastic fracture and limit load methods. Note that applying the instantaneous stress as a constant stress is conservative because a small amount of plastic deformation will redistribute the peak loads and reduce the stresses significantly. Treating impact stresses as constant stresses implies that they are applied long enough to cause complete failure if they are high enough magnitude.

The lid seal weld is 18.9 mm thick and it is loaded by bending stresses of magnitude +/-250 MPa (Figure 17). This geometry and loading were approximated using the *J*-integral solution for the single-edge cracked plate in three-point bending (Kumar et al. 1981). Figure 18 shows the *J*-integral curves for 200, 225, 250, and 275 MPa bending stress. The *J*-resistance curve was shifted along the crack depth axis until it became nearly tangent with the *J*-integral curve for 250 MPa bending stress. This result corresponds to a flaw depth of approximately 9.6 mm. The critical flaw depth based on limit load analysis was approximated by equating the plastic hinge moment at the flawed section to the bending moment in the unflawed section. Figure 19 shows a schematic of this condition along with the bending stress vs. critical flaw depth curve. The critical depth at 250 MPa bending stress is calculated to be 4.8 mm, or 1/2 the critical depth from the elastic-plastic fracture evaluation.

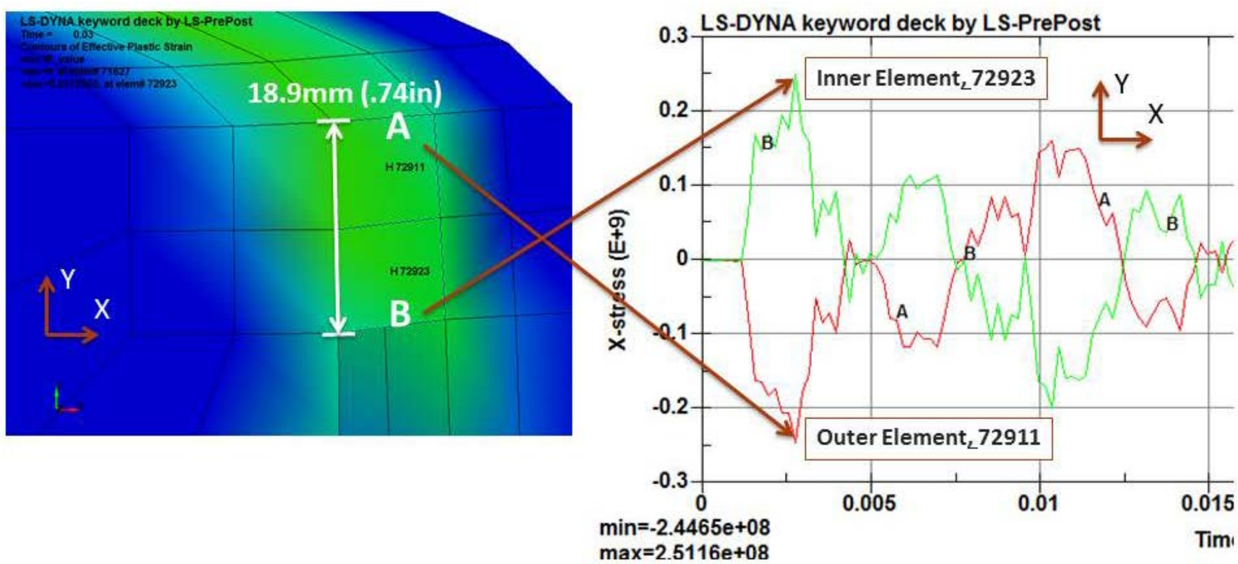

Figure 17: Radial Stress History through Canister Lid Seal Weld (Path A to B) during Impact

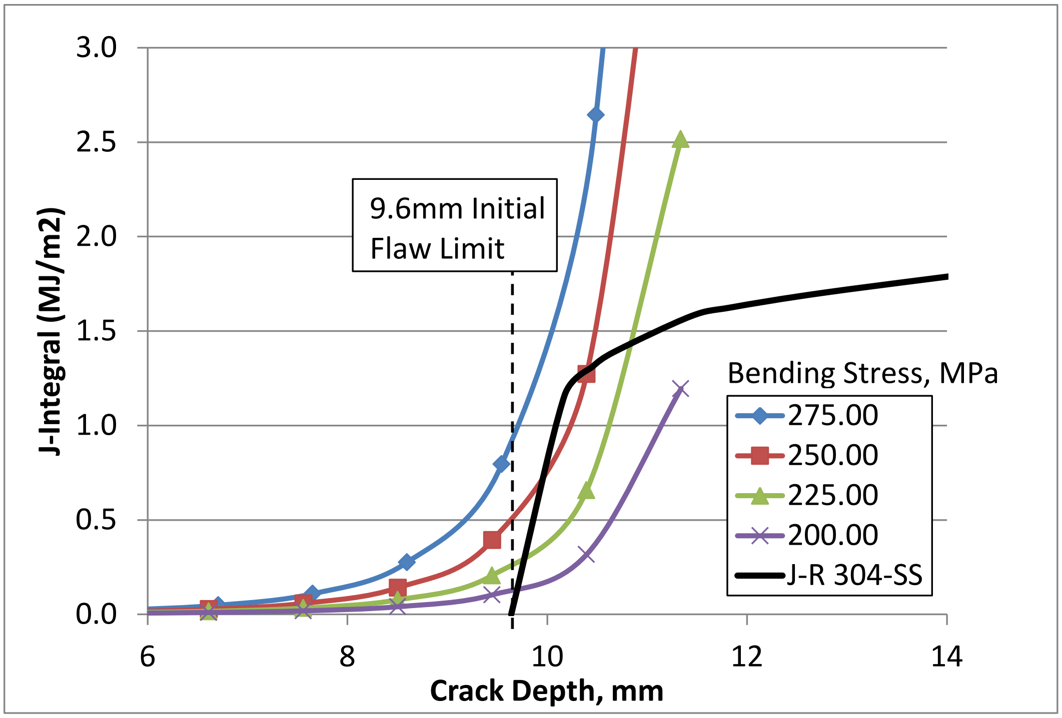

Figure 18: *J*-integral vs. *J*-resistance Curves for Canister Seal Weld under +/-250 MPa Bending Stress

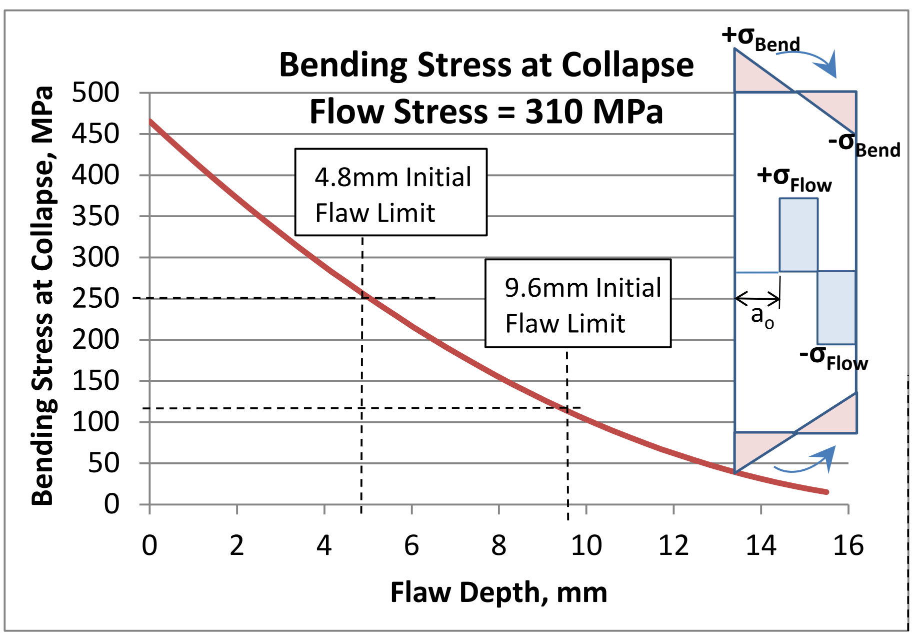

Figure 19: Bending Stress in the Uncracked Section that Results in a Plastic Hinge through the Remaining Ligament for the Corresponding Flaw Depth

Shear stresses through the weld section were also evaluated. The flow stress in shear from von Mises yield theory is the tensile flow stress divided by $\sqrt{3}$ (i.e., 310 MPa / $\sqrt{3}$ =179 MPa). Figure 20 shows the shear stress history through the canister lid seal weld section. The maximum average shear stress is about 145 MPa at 0.0025 seconds into the transient. Figure 21 plots the average shear stress in the uncracked section vs. flaw depth that corresponds to the 179 MPa shear flow stress in the remaining ligament. A flaw depth of 3.8 mm gives 179 MPa shear in the remaining ligament with 145 MPa shear in the uncracked section. Comparing the critical flaw depths from elastic-plastic fracture in bending (9.6 mm) to the limit load in bending (4.8 mm) to the average shear limit (3.8 mm) shows that shear is governing. Note that 3.8 mm is 20% of the 18.9 mm section thickness of the lid seal weld.

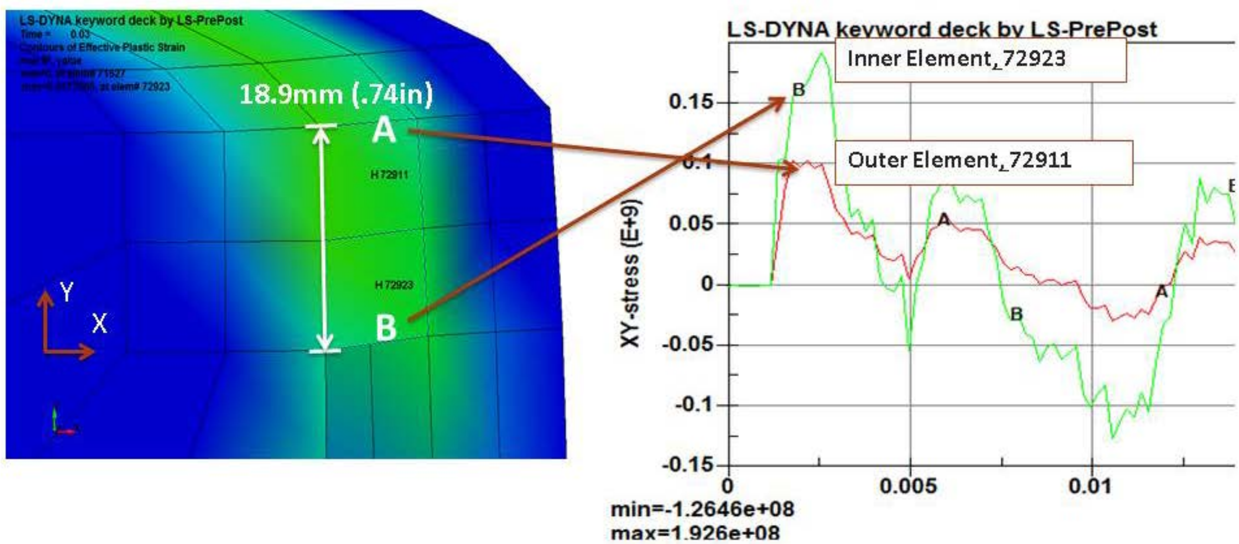

Figure 20: Shear Stress History through the Canister Lid Seal Weld Section during Impact Loading

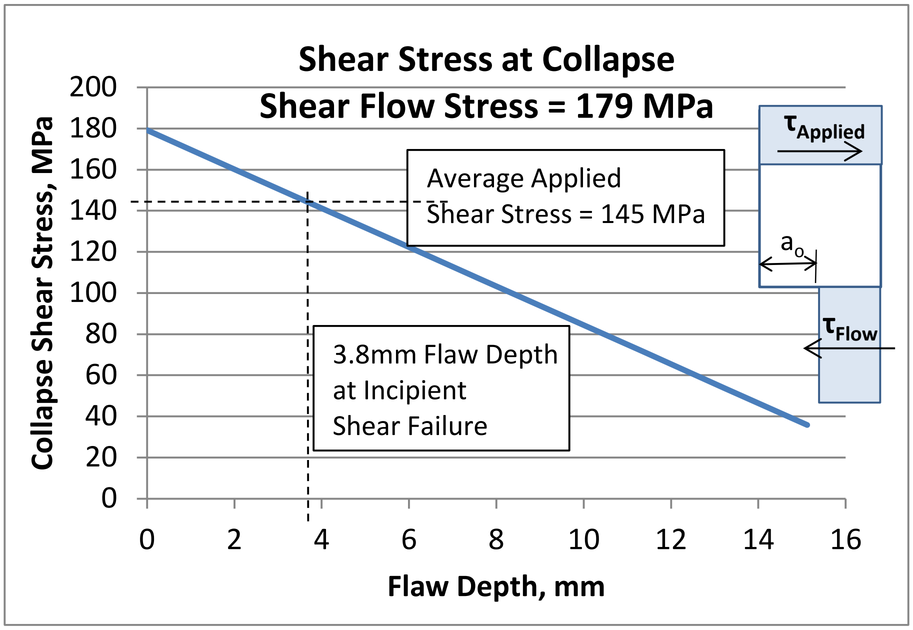

Figure 21: Shear Stress in the Uncracked Section that Corresponds to the 179 MPa Shear Flow Stress in the Remaining Ligament of the Corresponding Flaw Depth

This canister weld evaluation demonstrates that all critical loads and failure modes must be evaluated to determine which governs failure. These calculations are, in general, conservative because they evaluate peak dynamic stresses with static stress-based failure criteria. In Section 3.3.3 below, alternate strain-based failure analysis methods are described that compare the maximum strains from finite element impact models with rupture strain limits that account for the triaxial state of stress during deformation.

Full 360º circumferential flaws are also assumed in the analysis, which are of low probability for either fabrication-induced flaws or CISCC. MPC welds are typically performed in a number of passes—for example, three weld passes to complete a deep weld. Elastic-plastic fracture mechanics could therefore be used to determine that a weld flaw must be greater than 1/4, 1/3 or 1/2, etc. of the weld depth for through-wall failure to occur for a given dynamic loading scenario. With multi-pass welds, this means that a flaw has to occur at the same location in multiple passes to build up a weld flaw that threatens the containment boundary. Deeper and longer flaws mean there is an easier chance of finding them during weld inspection.

3.3 An Overview of CISCC Research and Methods for Assessing Its Effect on the Structural Integrity of Welded MPCs

This section provides an overview of the research on CISCC of MPCs for used fuel storage. This work is summarized to identify the potential for and the consequences of this degradation mechanism to assess how it should be included in structural integrity evaluations of MPCs. This review covers the following topic areas:

- Susceptibility and significance of CISCC
- MPC weld residual stress research
- Structural assessment methods for normal and accident load conditions

3.3.1 The Susceptibility and Significance of CISCC on Canister Boundary Integrity

The U.S. Nuclear Regulatory Commission (NRC) has sponsored detailed studies on SCC of stainless steels used in dry storage containers. NUREG/CR-7030 (Caseres and Mintz 2010) studied SCC of 304 and 316 stainless steels in the presence of chloride salts (simulated sea salt, reagent grade sodium chloride, magnesium chloride, and natural sea salt collected near Corpus Christi, Texas). Both unwelded and welded U-bend specimens were held under high bending stress, sprayed with salt solution, allowed to dry, and exposed to controlled temperature and high-humidity conditions. Conditions that allowed the salt to deliquesce (i.e., form a brine solution on the sample) resulted in significant corrosion and SCC after 32 weeks (304 stainless steel) and 128 weeks (316 stainless steel).

NUREG/CR-7170 (He et al. 2013) performed further exposure testing to better understand the NUREG/CR-7030 findings in light of other studies that reported CISCC at lower salt concentrations, lower humidity, higher temperature, and lower stress/strain conditions. NUREG/CR-7170 also tested for SCC with non-chloride salts, including ammonium sulfate [$(NH_4)_2SO_4$], ammonium nitrate (NH_4NO_3), ammonium bisulfate (NH_4HSO_4), and fly ash leached in deionized water. No cracks were observed on specimens exposed to any of the non-chloride salts, even when the test humidity was above the deliquescence relative humidity.

Under the UFDC, DOE has sponsored research on SCC of stainless steels used in dry storage canisters. Enos et al. (2013) measured the chemistry of dust samples collected from canisters at the Calvert Cliffs interim storage facility. The chemical analysis showed the dust to be:

- Largely calcium sulfate, with chlorides present in only trace amounts
- The sodium and chloride concentrations were low despite close proximity to Chesapeake Bay
- Largely from inland sources

Enos et al. (2013) points out that the test conditions used in the SCC testing programs may be very conservative. The test conditions may not represent field conditions for several reasons:

- Sea salt may not represent the dust on the container surfaces
- Exchange with atmospheric gases was limited in the controlled experiments
- Other components in the dust may either reduce or increase the corrosivity of deliquesced brines

Enos et al. (2013) also present concentration maps of chemicals found in precipitation around the United States. These maps are from the National Atmospheric Deposition Program (NADP), National Trends Network (http://nadp.sws.uiuc.edu/data/NTN/). The NADP website also allows downloading the concentration data measured at specific locations. The chemicals measured include: Calcium (Ca^{2+}), Magnesium (Mg), Potassium (K), Sodium (Na), Ammonium (NH_4^+), Nitrate (NO_3^-), Chlorine (Cl), and Sulphate (SO_4^{2+}). The pH is also listed in the database. In addition, the Environmental Protection Agencies Clean Air Status and Trend Network (CASTNET) data base provides the concentration of Cl suspend in the local air mass. The NADP and CASTNET data bases can be used in conjunction to estimate the inventory of atmospheric contaminants in a region (EPRI 2006; EPRI 2015). In addition, it has been shown that atmospheric contaminant concentration can be modeled to provide estimates of the site specific contaminant concentration (Jensen et al 2016).

Overall, the CISCC experimental studies show that controlled temperature and humidity conditions can be imposed that will cause stainless steels to stress corrosion crack in the presence of concentrated chloride salts. However, the studies do not identify specific examples where these aggressive conditions exist at any interim storage facilities. SCC does not occur at temperature and humidity conditions where salt will not deliquesce. In addition, the actual surface contaminants at real locations may not be the right chemistry to promote SCC.

The following reports reflect the Electric Power Research Institute (EPRI)'s recent and significant research on the causes and effects of CISCC on spent fuel canisters:

- *Failure Modes and Effects Analysis (FMEA) of Welded Stainless Steel Canisters for Dry Cask Storage Systems* (EPRI 2013).
- *Calvert Cliffs Stainless Steel Dry Storage Canister Inspection* (EPRI 2014a).
- *Literature Review of Environmental Conditions and Chloride-Induced Degradation Relevant to Stainless Steel Canisters in Dry Cask Storage Systems* (EPRI 2014b).
- *Flaw Growth and Flaw Tolerance Assessment for Dry Cask Storage Canisters* (EPRI 2014c).
- *Susceptibility Assessment Criteria for Chloride-Induced Stress Corrosion Cracking (CISCC) of Welded Stainless Steel Canisters for Dry Cask Storage Systems* (EPRI 2015).

The FMEA considered the detectability and likelihood of these corrosion mechanisms occurring to rank the probability of through-wall crack penetration combined with the severity of the consequences. The goal was to focus resources on the most important mechanisms. The FMEA identified the credible degradation mechanisms, in order of likelihood, as 1) CISCC, 2) pitting, 3) crevice corrosion, 4) microbiologically induced corrosion, and 5) intergranular attack (EPRI 2013). CISCC was estimated to have the greatest potential for causing through-wall penetration of the confinement boundary. Other less likely modes include a gross corrosion defect and the rupture of a part-depth or through-wall crack. The overall probability of occurrence for these failure mechanisms is predicated on there being tensile surface stresses (residual plus applied) plus the right chloride-rich chemistry and humidity conditions existing on the surface of the canister.

Inspection of dry storage canisters at the Calvert Cliffs interim storage facility (EPRI 2014a) used remote sensing methods to measure canister temperatures and surface contaminants. Chemical analysis of surface contaminants reported low chloride concentrations that resembled inland rainwater more than seawater, indicating that the Calvert Cliffs local environment is influenced more by inland, rather than marine, air currents. This finding is consistent with the dust samples collected by Enos et al. (2013) from canisters at the Calvert Cliffs interim storage facility.

EPRI's literature review on the susceptibility of welded stainless steel canisters to CISCC included 1) industrial experience on stainless steel corrosion at near ambient temperature (25ºC – 80ºC), 2) ranking of corrosion modes for the potential to penetrate the canister boundary, 3) variation in corrosion initiation and growth rates for different material compositions and environmental conditions, and 4) characterization of deposited salts and other contaminants vs. time, temperature, geographic location, and canister geometry conditions (EPRI 2014b). The study found that pitting corrosion typically initiates under less aggressive conditions but that CISCC can propagate at a significantly higher rate.

The objectives of EPRI's flaw growth and flaw tolerance assessment were to 1) estimate the growth rates of CISCC cracking, 2) evaluate the effect of different ambient environments on crack growth rates, 3) calculate the mechanical flaw tolerance of the canisters, and 4) estimate the time for air to displace the inert atmosphere inside the canister (EPRI 2014c). A stress corrosion cracking rate model grew cracks in a range of atmospheric conditions, and ASME Section XI, Appendix C limit load analysis was used to estimate the critical flaw sizes for different canister designs (ASME 2013a). Assuming a small initial crack, the time to propagate a flaw through-wall varies greatly (26.5 to 81.3 years) depending on the temperature, surface chemistry, and humidity. The canister designs were estimated to be very flaw tolerant, with large flaws required before a critical flaw size is approached. However, Lam et al. (2014, 2015) show that the API/ASME 579 Fitness for Service method, which includes the effect of residual stresses on crack stability, gives critical flaw sizes that are roughly one-half the limit load method employed by ASME Section XI, Appendix C (ASME 2013a).

EPRI developed susceptibility assessment criterial to numerically rank welded stainless steel canisters within independent spent fuel storage installations for CISCC inspection (EPRI 2015). Four conditions are required for CISCC: 1) a stainless steel alloy that is susceptible to CISCC, 2) a sufficient concentration of chlorides on the canister surface, 3) surface temperature and humidity required for deliquescence of chloride salts, and 4) sufficient tensile stress at the canister surface. An example provided in the report (EPRI 2015) of a canister with relatively high ranking is one that:

- Is close to a marine shore
- Is on a site with a high yearly average absolute humidity
- Is on a site near a saline cooling tower and a salted road
- Has been in service for a relatively long time
- Has a relatively low decay heat
- Uses a material that is less resistant to CISCC initiation

3.3.2 MPC Weld Residual Stress Research

Under UFDC funding, Sandia National Laboratories (SNL) has fabricated a full-diameter cylindrical mockup of an interim storage canister to assess the effects of manufacturing processes on the residual stresses and material microstructure in the welded and unwelded regions of the cylindrical wall section (Enos and Bryan 2015). The mockup was produced using the same plate bending and welding processes used to fabricate the spent nuclear fuel canisters currently in service. After fabrication, two smaller pieces were cut from the mockup for material characterization studies. Residual stresses are being measured in the larger remaining piece. Deep-hole drilling, the contour method, and x-ray diffraction are being used to characterize different aspects of the residual stress distribution in the base metal, heat-affected zone, and the weld metal. Initial results show that residual stresses in the unwelded region are dominated by plate bending methods to form the cylindrical sections. Except for the near-surface regions, plate rolling results in tensile stress in the outside half of the wall and compressive stress on the inside half. Measurement of residual stresses in the welds and heat-affected zones is in progress. Metallurgical testing is also being performed to determine the level of welding-induced sensitization in the heat-affected zone, which is known to exacerbate CISCC.

NRC has performed a finite element modeling study to help quantify the magnitude of residual stresses in canister geometries (Kusnick et al. 2013). Table 1 of Kusnick et al. (2013) provides an interesting summary of actual CISCC events that have been found in nuclear power plant components exposed to atmospheric conditions near bodies of salt water. The NRC report also references joint NRC/EPRI round-robin comparisons of finite element residual stress models (references 6-10 in Kusnick et al. 2013). Those works focused on primary water SCC of dissimilar metal welds in a pressurizer surge nozzle geometry, whereas Kusnick et al. (2013) models the typical geometry of welds in the baseplate, wall, and lid of an MPC. For the axial and hoop welds in the body of the canister, the weld models predict that tensile stresses are in-line with the weld direction, and they decay rapidly within about 40 mm from the weld centerline. Therefore, CISCC cracks would be expected to grow perpendicular to the weld centerline in a zone extending to about 40 mm from the weld centerline. This expectation is consistent with the experimental work of Prosek et al. (2014) who found stress corrosion cracks growing perpendicular to the direction of tensile stress near welds. Similarly, the stresses near the baseplate and lid seal welds also become compressive at a small distance from the weld centerline. The model results help to identify the likely direction and location of cracks, and they predict that sufficiently high residual stress may be present in the canister welds and heat-affected zone to allow CISCC to initiate and potentially grow through-wall, if a corrosive environment is present.

Lam and Sindelar (2015) use the residual stress approximation methods in Appendix E of the API/ASME 579 Fitness for Service approach (2007) to account for residual stresses in crack stability calculations for an MPC. They also calculate the highest residual stresses to be parallel to the weld line (i.e., cracks oriented perpendicular to the weld line) for both the circumferential and axial welds.

3.3.3 Structural Assessment Methods for Canister Normal and Accident Load Conditions

This section reviews the structural assessment methods that are used to evaluate CISCC in MPCs. The recent studies evaluate CISCC driven by residual plus normal operating stresses to estimate the size and location of CISCC cracks, when they are likely to grow through-wall, and what will be the consequences on the spent fuel of losing the inert atmosphere (EPRI 2014c, Lam and Sindelar 2015). The normal deadweight and static pressure loads typically give stresses that are low compared to the welding residual stresses. Both the ASME Section XI Limit Load method (ASME 2013a) and the API/ASME 579 Fitness for Service method (API/ASME 2007) are stress-based methods, which are appropriate for sustained, normal loading conditions. As noted previously, Lam and Sindelar (2015) show that including residual stresses in the API/ASME 579 method gives critical flaw sizes that are roughly one-half those calculated using the limit load method in ASME Section XI, Appendix C (ASME 2013a).

For accident loads such as dynamic impact, the question of what assessment criteria to use is more complicated. NUREG-1864 (Malliakos 2007) used the LS-DYNA finite element code to perform dynamic impact analysis of a canister. The weld fracture analysis compared the maximum equivalent plastic strains from the impact model with test data on the strain to failure of the canister material. Strain-to-failure tests were performed on 308-SS test specimens that were taken from welds in nuclear reactor process piping constructed at the Savanna River Site in the 1950s. The piping was primarily 304 stainless steel with 308 stainless weld filler metal. The mean reduction of area (RA) in the tensile tests was 59.7% with standard deviation of 9.1%. Adjusting for temperature and strain rate, they used a mean RA = 52%, with standard deviation of 9.7% to calculate the maximum effective plastic strain at failure.

The maximum equivalent plastic strains from the finite element analysis were divided by the ductility factor to account for the triaxial state of stresses on material ductility. The ductility ratio, *DR*, is the failure strain under combined stress divided by the uniaxial failure strain. Based on strain-to-failure tests of ductile materials under different stress combinations, Manjoine (1982) relates the ductility ratio to the triaxiality factor as:

$$DR = 2^{(1-TF)} \tag{7}$$

where the triaxiality factor, *TF*, is defined as:

$$TF = \frac{\sigma_1 + \sigma_2 + \sigma_3}{\frac{1}{\sqrt{2}}\left[(\sigma_1 - \sigma_2)^2 + (\sigma_2 - \sigma_3)^2 + (\sigma_3 - \sigma_1)^2\right]^{1/2}} \tag{8}$$

The numerator of *TF*, $\sigma_1 + \sigma_2 + \sigma_3$, is the sum of the three principal stresses (three times the hydrostatic stress), and the denominator is the von Mises effective stress. The relationship of TF to the ductility observed in tests is as follows:

- TF = 1.0 corresponds to uniaxial tension ($\sigma_1 = \sigma_{eq}$).
- TF > 1.0 corresponds to stress states that constrain plastic flow and reduce the equivalent plastic strain to failure.
- TF < 1.0 corresponds to stress states that enhance plastic flow and increase the equivalent plastic strain to failure.

Figure 22 shows the ductility ratio vs. triaxiality for several materials under different stress combinations (Manjoine 1982). Note that the ductility ratio is truncated at a value of 2 for TF ≤ 0.

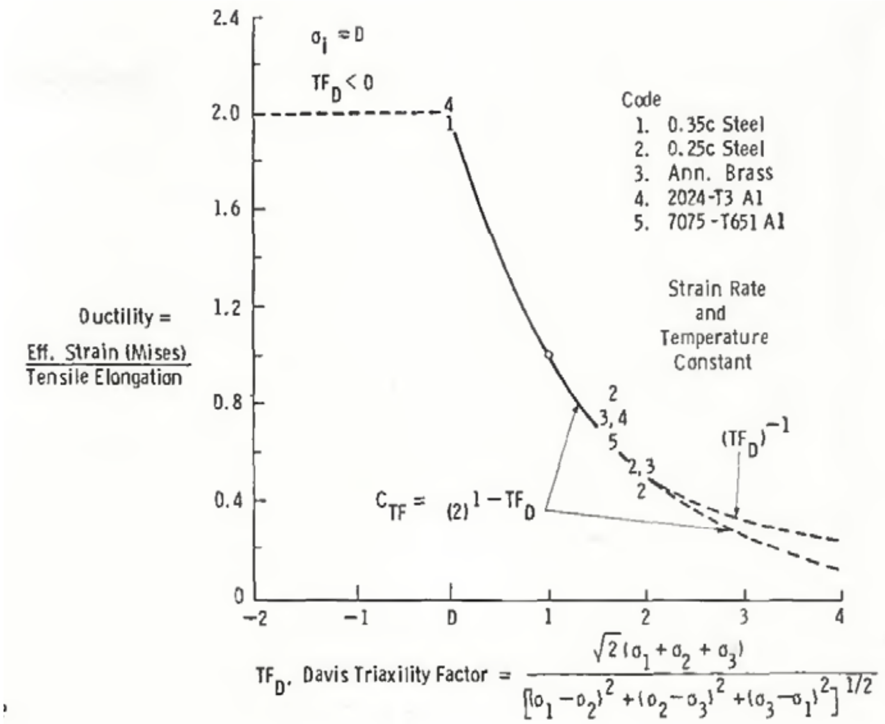

Figure 22: Ductility Factor vs. Stress Triaxiality Factor (Manjoine 1982)

Snow et al. (2009) present a strain-based acceptance criteria under consideration by ASME for application to one-time, energy-limited events such as accidental drops and impacts. For locations at least three wall thicknesses away from a local discontinuity the maximum strain, ε_{max}, is limited to $\varepsilon_{\max} \leq (0.67\varepsilon_{uniform})/TF$ where $\varepsilon_{uniform}$ is the strain at the onset of necking in a uniaxial tension test. For locations less than three wall thicknesses from a gross discontinuity, the strain limit is increased to $\varepsilon_{\max} \leq (0.85\varepsilon_{uniform})/TF$; however, these criteria do not apply to containment boundary fillet welds or partial penetration welds. Figure 23 compares the proposed strain criteria with the ductility factor for a range of triaxiality factors.

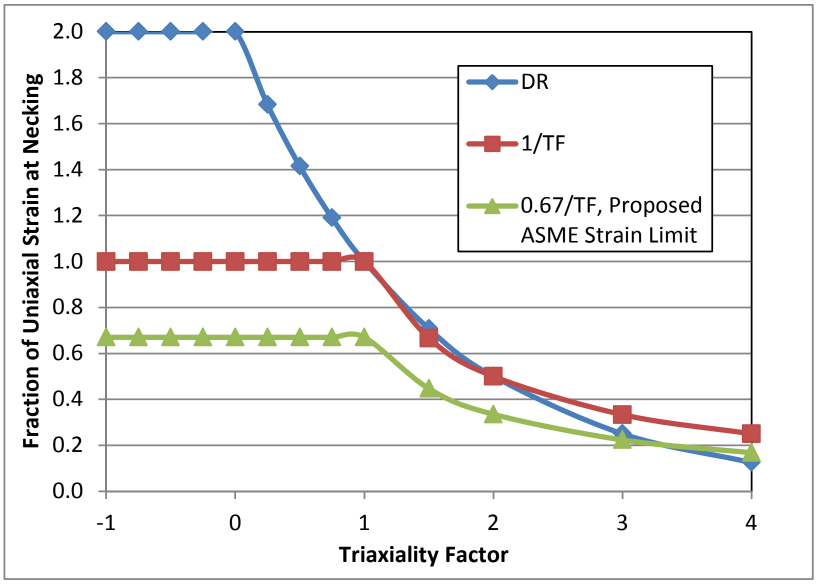

Figure 23: The Ductility Factor Compared to 1/TF and the 0.67/TF Limit Proposed by Snow et al. (2009) for the ASME Code

To account for the effects of stress triaxiality on the strain-to-failure, the effective plastic strains can be divided by the ductility ratio to calculate an adjusted strain for comparison with the uniaxial tensile strain limit. Malliakos (2007) used this method to evaluate weld strains from impact loading. No initial flaws were considered in this analysis.

PNNL extended the work of Malliakos (2007) by considering the effect of wall thinning due to CISCC (Klymyshyn et al. 2015a). A canister tip-over accident was modeled to estimate the significance of SCC on the integrity of welds in an MPC for long-term storage of UNF assemblies. The analysis assumed that SCC had occurred to a crack depth of one-half the canister wall thickness. A detailed finite element model of the canister geometry including the mass of the contained fuel was used to estimate the plastic strains from the tip-over accident. The model was first run without weld flaws to identify where SCC damage might be the most significant. Two locations in the lid seal weld and three locations in the circumferential base plate weld were identified for further damage analysis. The magnitude of effective plastic strain was used as the primary damage level criteria. The triaxial stress state during plastic deformation was also evaluated to calculate adjusted plastic strains for comparison with the estimated tensile elongation strain of 40%.

SCC flaws were simulated by removing elements along the weld line that represented 50% of the wall thickness. However, introducing this damage in the lid seal weld did not increase the previous maximum 39% strain in the impact zone of the lid seal weld. The maximum plastic strain occurred in the impact zone where net compression tends to increase the local rupture strain compared to the uniaxial tensile failure strain that is typically reported for ductile materials. Although the strains are much lower in other areas of the lid and base plate welds, the analysis showed that introducing weld damage can change the effective plastic strains and the local stress distributions enough to affect the local strain-to-failure.

Lam et al. (2014) proposed a framework for using the stress-based API/ASME 579 method to assess CISCC flaws under impact loading. Starting from the equivalent plastic strain reported in NUREG-1864 (Malliakos 2007), they suggest that the corresponding equivalent stresses could be estimated using the stress-strain curve for the specific canister alloy. Those stresses would then be used in API/ASME 579 (2007) to calculate the critical flaw sizes for those loadings. No example is provided to judge what critical crack size would be calculated for these stresses. NUREG-1864 only presents the equivalent plastic strains rather than the complete stress and strain history for the impact event. However, if the complete event were available for review, it is uncertain what the appropriate time during impact would be the most appropriate for evaluation. API/ASME 579 assumes continuous primary stresses that if high enough would directly result in failure. Choosing the peak stress could be too conservative because small plastic strain may reduce the peak stresses without causing failure. However, the plastic strains available from NUREG-1864 are the final result after impact. Depending on the magnitude and duration of the stresses and strains, these may not be conservative enough. To rely on the validity of the predicted final strains after impact, one must confirm that the constitutive model used in the computer analysis is capable of correctly simulating necking and failure at high stresses, strains, and strain rates.

3.4 Conclusions and Future Work

The probabilistic material failure relationship discussed in Section 3.1 is a potentially useful approach to evaluating MPC weld failure. Testing a million samples of MPC weld material is not feasible, but testing 100 samples of weld material for the purpose of developing a solid statistical basis for failure is a possibility. It is recommended that the statistical nature of material failure be considered in more depth as the Structural Uncertainty task continues.

The elastic-plastic fracture mechanics methodology discussed in Section 3.2 demonstrates that all critical loads and failure modes must be evaluated to determine which one governs failure. The methodology can provide assurance that a flaw of a certain size cannot cause failure under a certain dynamic load, but the methodology was developed for static loading conditions and is potentially conservative for dynamic loads. The transient aspect of dynamic loading means that certain short duration loads could potentially cause a crack to advance (gain in length) but not advance all the way through the wall thickness to violate the containment boundary.

Additional study and literature review is recommended on the structural assessment methods discussed in Section 3.3.3. The work of Lam and Sindelar (2015) was reviewed near the end of this project year. Their comparison of the API/ASME 579 (2007) evaluation methods and ASME Section XI, Appendix C (2013a) methods reveals that the inclusion of residual stresses in API/ASME 579 Fitness for Service calculates smaller critical crack depths than the ASME limit load method in Section XI, Appendix C. PNNL’s analyses to date have viewed residual stresses as self-equilibrating stresses that contribute to CISCC but do not contribute to failure under normal pressure, deadweight and thermal loads, or accidental impact loads. Therefore, PNNL proposes to further compare our methods in FY 2017 with the API/ASME 579 Fitness for Service methods and results reported by Lam and Sindelar (2015). The goal of this work will be to understand the underlying assumptions and differences in the methods and results to resolve what are the most appropriate failure criteria to apply to the evaluation of both static and dynamic loads on MPCs.

4.0 USED FUEL LOADING ESTIMATES

The UFDC program has a number of modeling and testing activities that are working to close the cladding stress and strain knowledge gap. This section offers a summary of the loads based on recent finite element modeling activities.

4.1 NCT Free-Drop Loaded Package Estimate

UNF packages are certified for NCT based on the tests described in 10 CFR 71.71 (NRC 2010). One test is a free drop of a loaded package onto an unyielding surface from a height that is specified according to the package mass. Typical package testing considers a number of angles of impact with the unyielding surface to ensure the most limiting conditions are tested. This type of testing is specified to demonstrate the package's ability to maintain the containment boundary around the used fuel. 10 CFR 71.71 governs the package, not UNF, but it does provides a basis for evaluating UNF response to impact loading conditions that the package is expected to survive.

The ENSA ENUN 32P package was modeled in Klymyshyn (2016a) for horizontal free-drop conditions. A range of fuel rod bending rigidities was evaluated to account for a range of temperature, burnup, and fuel-to-cladding bonding. The temperature range was 22°C to 300°C, the burnup range was 10 GWd/MTU to 55 GWd/MTU, and the amount of fuel-to-cladding bonding was 0% (empty cladding) to 100% (cladding and fuel perfectly bonded). The maximum upper bound on strain was calculated to be 0.003025, which includes a stress concentration factor of 1.38 on the cladding to represent localized stress that is expected to occur at the interface between fuel pellets.

A generic rail and truck cask were modeled in Klymyshyn (2016b) to study the effect of geometry variation during a 30 cm free drop. The amount of gap existing between the fuel assembly and the basket wall at impact was the main geometry variable that was studied, but 1°off-horizontal impact cases were also considered. This study fixed the fuel configuration as 22°C, 10 GWd/MTU burnup, and 50% fuel stiffness contribution to fuel rod EI. The maximum axial cladding strain was calculated to be 0.014511, which is above the yield strain of 0.011027 but below the failure strain of 0.015574. This case includes stress concentration factor of 1.38 as well as a factor to account for the possibility of missing the peak strain between recorded solution states.

The relatively high strains calculated in Klymyshyn (2016b) are caused by the maximized gap condition and represent the response when the fuel assembly happens to be located at the top of the fuel compartment at the time of impact. This is considered to be a highly conservative configuration because an actual free-drop test scenario (performed according to 10 CFR 71.71 [NRC 2010]) would have the fuel assembly aligned with the bottom of the fuel compartment at the time of release. The fuel assembly has the freedom to move within the fuel compartment because the compartment has more available space than the fuel assembly occupies, but there is no reason to suspect that the fuel assembly would be at the maximum gap configuration under free-drop test conditions. The maximum gap condition was studied to determine the maximum possible loads on the fuel assembly, but it is not clear that such a configuration would be possible considering normal free-drop test conditions and possible realistic handling drop conditions.

A similar rail and truck package 30 cm free-drop analysis was described in Klymyshyn (2016c), but in this case the geometry was fixed and the EI of the UNF was varied. The temperature ranger was 22°C to 300°C, the burnup range was 10 GWd/MTU to 90 GWd/MTU, and the amount of fuel-to-cladding bonding was 0% (empty cladding) to 100% (cladding and fuel perfectly bonded). This study determined a peak nominal cladding strain of 0.002001, which was based on a peak instantaneous bending moment of 6.8 N-m. This case considered a minimum gap at impact (less than 1 mm of separation between the fuel assembly and the fuel basket in the direction of initial velocity) and did not consider stress concentrations or other modeling uncertainty factors.

The NCT package drop analyses all tend to agree that the fuel rod EI assumption has an effect on the response of the fuel assembly and the calculated fuel cladding strain. However, they also agree that the variation in response caused by EI tends to be insignificant compared to the cladding yield strain. The one exception is the geometric sensitivity study that found the maximum gap case caused loads that exceeded the cladding yield strain limit and came close to reaching the cladding failure limit. In that case, the loads on the fuel were significant enough that the choice of EI was important.

Future work in this area is needed to explore NCT package drops at the full range of impact angles in order to fully explore the potential loading regime for NCT conditions.

4.2 NCT Highway Transportation Loading Estimate

In FY15, staff at PNNL developed a methodology that used the modeled structural transmissibility of an actual spent nuclear fuel conveyance (Klymyshyn et al. 2015b) to scale the SNL truck test data that was collected in FY14 (McConnell et al. 2014). The utility of this is that the resultant scaled data can then be used to compare the as-tested configuration to the untested spent nuclear fuel conveyance. The results of this analysis are shown in Figure 24. The original time history from the SNL testing is shown in red, and the new scaled time history that represents the untested spent nuclear fuel conveyance is shown in blue.

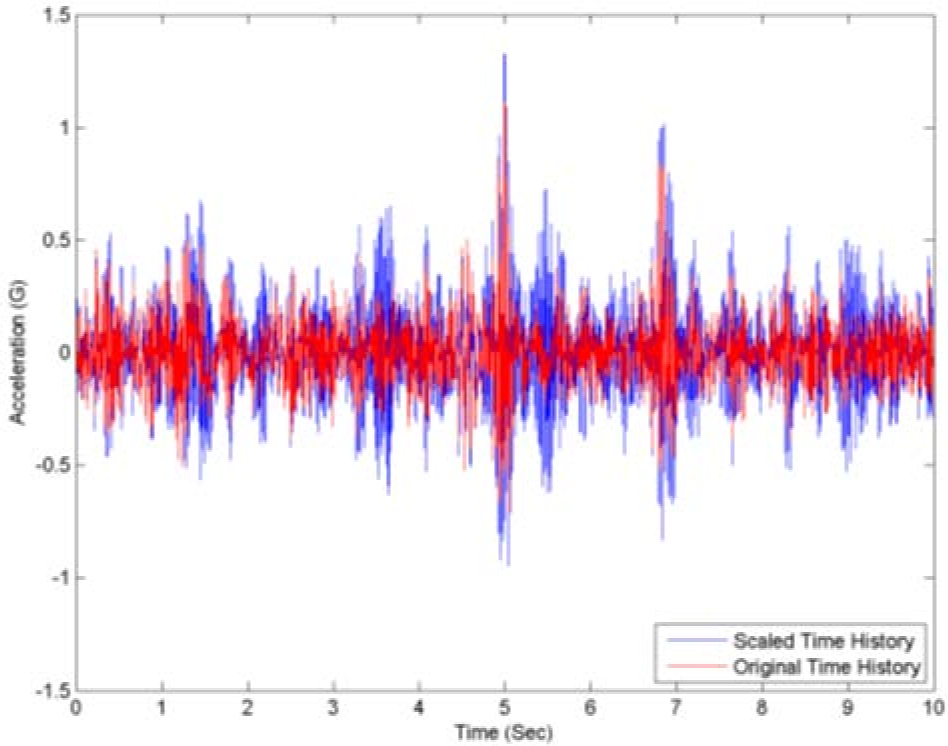

Figure 24: Scaled and Original Acceleration Time History

In FY16, the acceleration time histories shown in Figure 24 were used as an input to finite element models to better understand how actual spent nuclear fuel would perform under both scenarios. The results of this analysis were presented at the 18th International Symposium on the Packaging and Transportation of Radioactive Materials (Jensen et al. 2016) in Kobe, Japan, and are summarized herein.

PNNL often uses a detailed full fuel assembly finite element model in a number of dynamic loading applications, such as transportation package free drop impact evaluation (Klymyshyn et al. 2016), shock loading, and short duration vibration testing. The full fuel assembly model is not well suited to modeling behavior beyond 2 seconds of solution time because of the long computation times necessary to run it. This study considers a 10-second basket-loading window, which makes it a challenging problem for the full detailed fuel assembly model. It would take about 100 hours of calculation time to solve the model for 10 seconds of solution time. This study uses a limited finite element model of one fuel rod to determine if using the full fuel assembly is necessary. In this case, the loads are ultimately determined to be so small that using the full fuel assembly model is not necessary to determine the loads on the UNF.

The single fuel rod finite element model is sketched in Figure 25 and Figure 26. The full length of one fuel rod is represented with beam elements. Prescribed motion is applied at the nodes that are indicated in the sketch. A key assumption in this analysis is that the basket motion is directly applied to the fuel rod at the grid locations, which is a simplification that neglects the transmission of loads through the complex fuel assembly structure. This model also assumes the loaded fuel rod nodes maintain a horizontal orientation.

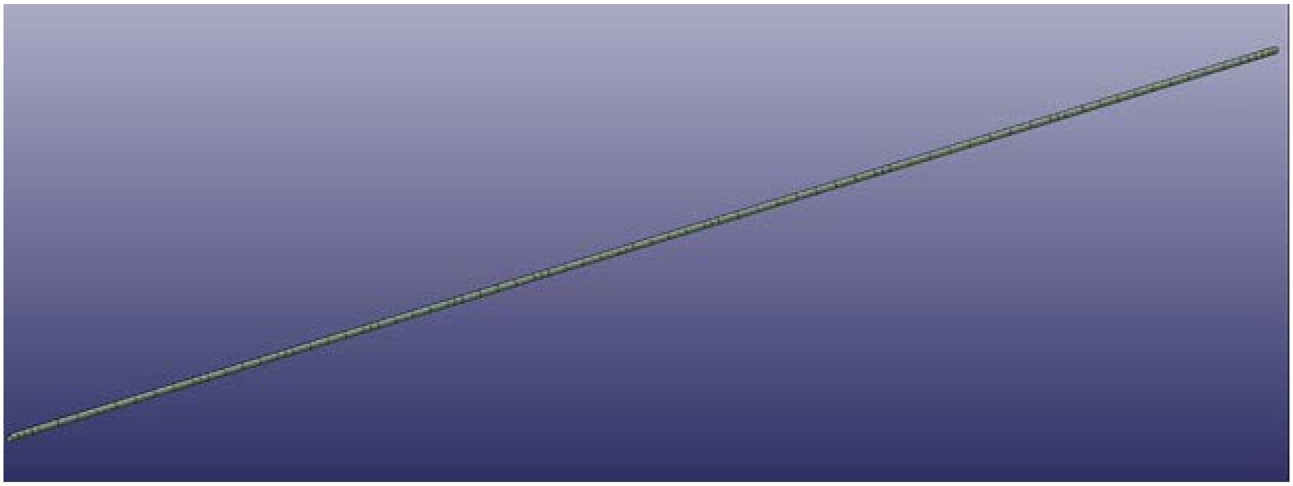

Figure 25: Isometric View Showing Mesh

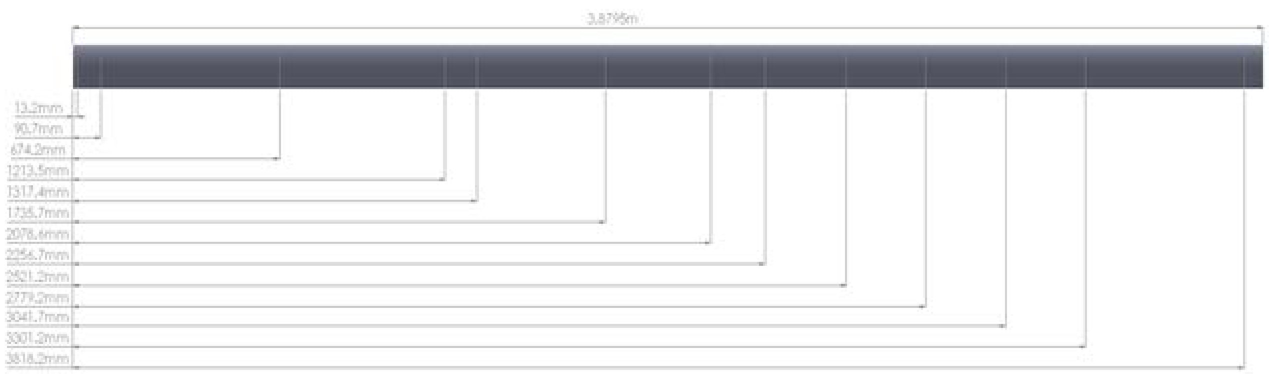

Figure 26: Rod Length and Loading Locations

All of the prescribed motion histories used in this study were derived from the SNL truck test. The raw acceleration load was filtered with a bandpass filter, with 1 Hz and 500 Hz cutoff frequencies to determine the acceleration history of interest. The peak acceleration was identified, and a ten-second window was taken from the filtered data. The applied motion causes transient inertia loads to develop in the fuel rod, causing the fuel rod to bow and vibrate in the unsupported spans between grid spacers. Gravity is active in the model and is applied and initialized over the first 0.1 seconds of solution time, prior to starting the applied motion histories.

The baseline model has a beam EI that represents empty zirconium alloy cladding, which approximates the as-tested cladding case that has lead rope within the cladding to represent the mass of fuel. This study also models the UNF with a beam EI that represents real UNF with a fraction of the fuel bonded to the cladding and contributing to the total EI. The cladding EI is 12.9 N-m^2, and the realistic used fuel is considered to have an EI of 31.38 N-m^2, which is a rough approximation of UNF with a burnup of 45 GWd/MTU.

The maximum axial strain calculated in the baseline model is 0.000597. This is the maximum integration point value through time. The LS-DYNA beam model uses the default Hughes-Liu element formulation with 3x3 Lobotto quadrature. The maximum integration point value is expected to be a close indicator of the local maximum cladding strain. This is generally comparable to the maximum strain gage data of approximately 0.000150 that was recorded during testing (McConnell et al. 2014). However, some differences are expected because the strain gage data is at fixed points on certain fuel rods and the current model only represents one fuel rod that is decoupled from interaction with spacer grids and neighboring fuel rods. Comparing 0.000150 to 0.000597, the single rod model provides a conservative estimate of the actual recorded response to truck transportation loads. The difference between 0.000150 and 0.000597 is an indicator of the relative significance of the fuel assembly details that were not modeled in this simplified analysis.

Another result that is reported is the maximum nodal deflection that occurs relative to the rigid body motion of the fuel rod grid locations. The nodes at the spacer grid locations all experience the same rigid body motion, but the nodes associated with the unsupported fuel rod span lengths are free to bow under gravity and the imposed dynamic loading. The maximum relative deflection is an indicator of the amount of mid-span bowing that occurs (i.e., the longest span is expected to have maximum deflection). The peak deflection in the baseline case is 1.66 mm. This result is small relative to the distance between fuel rods, which is generally reported to be 12.6 mm (Todreas and Kazimi 1990), and indicates that rod-to-rod interaction would not occur.

The highway amplified load was applied to the as-tested cladding model and the 45 GWd/MTU burnup UNF model, with EI and E as identified in Table 2. Full results are reported in Table 3. The peak strains were 0.000607 and 0.000137, respectively. The results show that adjusting the system dynamics to more closely represent an actual UNF conveyance results in a slight increase in the expected strains. Also, when the EI for high burnup UNF is used in the model, the peak strain is significantly reduced because the larger EI results in less rod deflection, which in turn results in lower axial strain.

Because the highway amplified load did not result in significantly higher strains or mid-span deflections than the baseline case, the amplified load was scaled up by a factor of 10 to demonstrate an unrealistically severe loading case. In this case, the resultant strains are increased to 0.004172 for the cladding case and 0.001616 for the UNF case. Both of these results are less than half the strain necessary to cause UNF to yield (McConnnell et al. 2014). The peak mid-span deflection indicates that rod-to-rod interaction may occur if two adjacent rods deflected in opposing directions. Also, for the amplified cases, the bending moment and shear force are increased by an order of magnitude.

Table 2: Flexural Rigidity (EI) and Elastic Moduli

	EI N-m^2	E in Model GPA
Cladding as tested	14.29	89.3
UNF 45 GWd/MTU	31.38	196.1

Table 3: Axial Strains, Peak Deflection, Shear Force, and Bending Moment

	EI	Load	Peak Axial Strain	Peak Deflection (mm)	Shear Force (N)	Bending Moment (N-m)
Baseline	cladding	Baseline	0.000597	1.66	18.02	1.91
Amplified	cladding	Amplifiedx1	0.000607	1.75	18.07	1.94
Amplified	UNF	Amplifiedx1	0.000137	0.38	9.01	0.91
Major Amp.	cladding	Amplifiedx10	0.004172	8.60	140.87	11.03
Major Amp.	UNF	Amplifiedx10	0.001616	3.26	107.92	9.59

4.3 Normal Conditions of Rail Transportation Loading Estimate

The current best estimate of NCT rail loading is a modeling study documented in Adkins et al. (2013). The magnitude of expected mechanical shock loading was estimated to be well within the range of survival for one application of the load. Potential fatigue damage was assessed for vibration and shock for a 3000-mile route, and the total projected damage was estimated to be 18%. Using this analysis method, failure is not expected for damage fractions less than 100%. The cumulative fatigue damage assessment is based on a lateral vibration damage fraction of 7% and a lateral shock damage fraction of 11%. Lateral shock and vibration were found to be the most limiting. Conservative assumptions were made regarding the amount of vibration and frequency of shocks that would occur during the 3000-mile trip. This assessment also represents the damage on the single most limiting fuel rod, so the average damage fraction throughout the fuel payload is expected to be somewhat lower that 18%. In general, this damage projection is expected to be highly conservative.

The ENSA/DOE rail testing to be completed in FY17 will provide an experimental testing basis to determine used fuel loading during rail transportation. The test results are expected to confirm that the potential for damage during rail NCT transport is low.

4.4 Conclusions and Future Work

All of the current modeling estimates predict that expected NCT loads on UNF will be relatively low, compared to the yield strength of cladding. One exception is the NCT package drop modeling that includes a maximized gap condition. The maximized gap condition is a conservative assumption because the free-drop testing described in 10 CFR 71.71 (NRC 2010) is not expected to cause a maximized gap condition. Realistic drop events, as might occur during actual package handling, are expected to be very situational in regards to the gaps that might develop. Assuming maximum gaps provides bounding loads, but it may be more worthwhile to consider the maximum credible gaps for NCT-level package drop events.

The fuel rod EI has been shown to make a difference in UNF response to NCT loads, but the range of response tends to be at a low magnitude that is not significant compared to the cladding yield strength. Lower-bound EI cases tend to respond with higher cladding strains and fuel rod deflections. Future work will continue to treat EI as a variable to consider the response of UNF within a realistic range of EI.

The NCT drop evaluations will be continued in FY 2017 to evaluate UNF loading under different impact angles. The goal is to fully bound the package free-drop test described in 10 CFR 71.71 (NRC 2010) to assess the loading environment associated with NCT free drops. Other impact angles are expected to be more complicated to model, and this modeling effort may take more time and effort than will be available in FY 2017.

The highway load transmissibility study described in Section 4.2 will be expanded to evaluate additional EI values to help determine under what loads the EI begins to make a significant difference. Similar load transmissibility modeling will be performed to support the ENSA/DOE rail test campaign in FY 2017.

5.0 CONCLUSIONS

This report summarizes work performed on the Structural Uncertainty task in FY 2016. This task will continue in FY 2017.

Valuable model validation data was collected on rod and cladding tube dynamic behavior to help with efforts to validate PNNL's detailed 17x17 pressurized water reactor finite element model. Future work will focus on using the data to validate LS-DYNA models and determine the most accurate way to model and post-process UNF using beam elements in LS-DYNA.

Methods for modeling failure in MPC welds were evaluated and a survey of current research in stress corrosion cracking was conducted. Future work will continue to evaluate failure criteria, including the API/ASME 579 Fitness for Service methods (2007). Statistical data related to weld material failure is another area for future work.

A number of related modeling efforts have recently been completed that help define the expected range of loading under NCT. The results were summarized in this report, and areas for additional modeling were identified. Additional NCT package drop evaluations will be completed to evaluate the full range of possible impact angles and the influence impact angle has on UNF loading. The effect of fuel rod EI will continue to be studied through modeling to help determine how important it is for material testing to precisely establish the EI of UNF.

6.0 REFERENCES

Adkins, HE, Jr, KJ Geelhood, BJ Koeppel, J Coleman, J Bignell, G Flores, JA Wang, SE Sanborn, R Spears, and NA Klymyshyn. 2013. *Used Nuclear Fuel Loading and Structural Performance Under Normal Conditions of Transport – Demonstration of Approach and Results on Used Fuel Performance Characterization*. FCRD-UFD-2013-000325.

API/ASME. 2007. *Fitness-for-Service.* API 579-1/ASME FFS-1, June 5, 2007. American Petroleum Institute and the American Society of Mechanical Engineers. API Publishing Services, Washington, D.C.

ASME. 2013a. ASME Boiler & Pressure Vessel Code, Section XI, *Inservice Inspection*, Appendix C. American Society of Mechanical Engineers. New York, New York.

ASME. 2013b. ASME Boiler & Pressure Vessel Code, Section II, Part D, *Properties, Materials*. American Society of Mechanical Engineers. New York, New York.

Caseres, L and TS Mintz. 2010. *Atmospheric Stress Corrosion Cracking Susceptibility of Welded and Unwelded 304, 304L, and 316L Austenitic Stainless Steels Commonly Used for Dry Cask Storage Containers Exposed to Marine Environments.* NUREG/CR-7030. Southwest Research Institute. San Antonio, Texas.

Enos, D and C Bryan, 2015. *Status Report: Characterization of Weld Residual Stresses on Full Diameter SNF Interim Storage Canister Mockup*. FCRD-UFD-2015-00123, SAND2015-7068 R. Sandia National Laboratories, Albuquerque, New Mexico.

Enos, DG, CR Bryan, and KM Norman. 2013. *Data Report on Corrosion Testing of Stainless Steel SNF Storage Canisters, Fuel Cycle Research and Development.* FCRD-UFD-2013-000324, SAND2013-8314. Sandia National Laboratories, Albuquerque, New Mexico.

EPRI. 2006. *Climactic Corrosion Considerations for Independent Spent Fuel Storage Installations in Marine Environments.* Report No. 1013524. December 2006. Electric Power Research Institute, Palo Alto, California.

EPRI. 2013. *Failure Modes and Effects Analysis (FMEA) of Welded Stainless Steel Canisters for Dry Cask Storage Systems.* Report No. 3002000815. December 2013. Electric Power Research Institute, Palo Alto, California.

EPRI. 2014a. *Calvert Cliffs Stainless Steel Dry Storage Canister Inspection.* Report No. 1025209. April 2014. Electric Power Research Institute, Palo Alto, California.

EPRI. 2014b. *Literature Review of Environmental Conditions and Chloride-Induced Degradation Relevant to Stainless Steel Canisters in Dry Cask Storage Systems.* Report No. 3002002528. May 2014. Electric Power Research Institute, Palo Alto, California.

EPRI. 2014c. *Flaw Growth and Flaw Tolerance Assessment for Dry Cask Storage Canisters.* Report No. 3002002785. October 2014. Electric Power Research Institute, Palo Alto, California.

EPRI. 2015. *Susceptibility Assessment Criteria for Chloride-Induced Stress Corrosion Cracking (CISCC) of Welded Stainless Steel Canisters for Dry Cask Storage Systems.* Report No. 3002005371. September 2015. Electric Power Research Institute, Palo Alto, California.

He, X, TX Mintz, R Pabalan, L Miller, and G Oberson. 2013. *Assessment of Stress Corrosion Cracking Susceptibility for Austenitic Stainless Steels Exposed to Atmospheric Chloride and Non-Chloride Salts*. NUREG/CR-7170. Southwest Research Institute. San Antonio, Texas.

Jensen, PJ, NA Klymyshyn, SB Ross, and PE McConnell. 2016. “Modeled Structural Transmissibility of a Used Nuclear Fuel Conveyance Applied to Over the Road Test Data and Finite Element Modeling.” In *Proceedings of the 18th International Symposium on the Packaging and Transportation of Radioactive Materials: PATRAM 2016*, September 18-23, Kobe, Japan.

Jensen, PJ, T Tran, BG Fritz, FC Rutz, SB Ross, AM Gorton, R Devanathan, P Plante, and K Trainor. 2016. “Preliminary Evaluation of the DUSTRAN Modeling Suite for Modeling Atmospheric Chloride Transport”, *Air Qual Atmos Health.* doi:10.1007/s11869-016-0404-5

Ji, W, YJ Chao, MA Sutton, PS Lam, and GE Mertz. 1993. “J-Integral of Circumferential Crack in Large Diameter Pipes.” *The Second ASME/JSME Nuclear Engineering Joint Conference*, Vol. 2, pp. 139-149. San Francisco, California.

Klymyshyn NA, PJ Jensen. 2016a. “Used Nuclear Fuel Rail Package Normal Conditions of Transport (NCT) Drop Analysis.” PNNL-25133, Pacific Northwest National Laboratory, Richland, Washington.

Klymyshyn, NA, NK Karri, HE Adkins, and BD Hanson. 2013. *Structural Sensitivity of Dry Storage Canisters.* FCRD-UFD-2013-000378. PNNL-22814, Pacific Northwest National Laboratory, Richland, Washington.

Klymyshyn, NA, NK Karri, HE Adkins, Jr, and BD Hanson. 2014a. *Structural Uncertainty of Used Nuclear Fuel in Dry Storage Canisters*. PNNL-23710, Pacific Northwest National Laboratory, Richland, Washington.

Klymyshyn, NA, NP Barrett, KI Johnson, and BD Hanson. 2015a. *Update: Structural Uncertainty of Used Nuclear Fuel in Dry Storage Canisters*. PNNL-24669, Pacific Northwest National Laboratory, Richland, Washington.

Klymyshyn, NA, PJ Jensen, and NP Barrett. 2015b. *Shaker Table Modeling Support Task 2015*. PNNL-24735, Pacific Northwest National Laboratory, Richland, Washington.

Klymyshyn, NA, PJ Jensen, and NP Barrett. 2016b. “Modeling Used Fuel Response to Normal Condition of Transportation Package Drops to Assess Geometric Sensitivities.” *American Nuclear Society Top Fuel 2016*, Boise, Idaho.

Klymyshyn, NA, PJ Jensen, and NP Barrett. 2016c. “Used Fuel Response 30cm Package Drops.” *PATRAM 2016,* Kobe, Japan.

Klymyshyn, NA, PJ Jensen, SE Sanborn, and BD Hanson. 2014b. *Fuel Assembly Shaker and Truck Test Simulation*. PNNL-23688, Pacific Northwest National Laboratory, Richland, Washington.

Kumar, V, MD German, and CF Shih. 1981. *An Engineering Approach for Elastic-Plastic Fracture Analysis.* EPRI NP-1931. Project 1237-1, Topical Report July 1981. Prepared for EPRI by General Electric Company, Schenectady, New York.

Kusnick, J, M Benson, and S Lyons. 2013. *Finite Element Analysis of Weld Residual Stresses in Austenitic Stainless Steel Dry Cask Storage System Canisters.* U.S. Nuclear Regulatory Commission, Washington, D.C.

Lam, PS and RL Sindelar. 2015. *Development of Flaw Acceptance Criteria for Aging management of Spent Nuclear Fuel Multi-Purpose Canisters*. PVP2015-45935. ASME, New York, New York.

Lam, PS, RL Sindelar, AJ Duncan, and TM Adams. 2014. *A framework to Develop Flaw Acceptance Criteria for Structural Integrity Assessment of Multipurpose Canisters for Extended Storage of Used Nuclear Fuel*. PVP2014-28990. ASME, New York, New York.

LSTC. 2013. *LS-DYNA® Keyword User's Manual, Volume II, Material Models*, Version R7.0, Livermore Software Technology Corporation, Livermore, California.

Malliakos, A. 2007. *A Pilot Probabilistic Risk Assessment of a Dry Cask Storage System at a Nuclear Power Plant.* NUREG-1864. U.S. Nuclear Regulatory Commission, Washington, D.C.

Manjoine, MJ. 1982. "Creep Rupture Behavior of Weldments." *Welding Journal: Research Supplement*, Vol. 61, No. 2, American Welding Society, Miami, Florida.

McConnell, PE, R Wauneka, S Saltzstein, and K Sorenson. 2014. *Normal Conditions of Transport Truck Test of a Surrogate Fuel Assembly*. Sandia National Laboratories, Albuquerque, New Mexico.

NRC, EPRI. 2011. *Models and Inputs Developed for Use in the xLPR Pilot Study.* U.S. NRC Office of Nuclear Regulatory Research, Washington, D.C. Electric Power Research Institute, Palo Alto, California.

NRC. 2010. *Normal Conditions of Transport*. 10 CFR Part 71.71, U.S. Nuclear Regulatory Commission, Washington, D.C.

Prosek, T, A Le Gac, D Thierry, S Le Manchet, C Lojewski, A Fanica, E Johansson, C Canderyd, F Dupoiron, T Snauwaert, F Maas, and B Droesbeke. 2014. "Low Temperature Stress Corrosion Cracking of Austenitic and Duplex Stainless Steels under Chloride Deposits." *Corrosion* 70(10):1052-1063.

Roark, RJ, and WC Young. 1975. *Formulas for Stress and Strain.* Fifth Edition. McGraw-Hill. New York, NY.

Sampath, SG, IS Abou-Sayed, D Broek, C Marshall, A Zahoor, and MF Kanninen. 1981. “The Analysis of Stable Crack Growth in Type 304 Stainless Steel.” Battelle Columbus Laboratories, Columbus, Ohio. In *Proceedings of Advances in Fracture Research, International Conference on Fracture*, Cannes, France, pp. 1759-1767.

Snow, SD, DK Morton, EL Pleins, and R Keeting. 2009. “Strain-Based Acceptance Criteria for Energy-Limited Events.” In *Proceedings of the 2009 ASME Pressure Vessels and Piping Division Conference*, July 26-30, 2009, Prague, Czech Republic.

Todreas, NE and MS Kazimi. 1990. “Nuclear Systems Volume 1: Thermal Hydraulics Fundamentals, First Edition.” Taylor & Francis Group.